Nucleic Acids Research, 2024, **52**, 5048–5066
https://doi.org/10.1093/nar/gkae140
Advance access publication date: 27 February 2024
Genome integrity, repair and replication

DNA-PKcs suppresses illegitimate chromosome rearrangements

Jinglong Wang *, Cheyenne A. Sadeghi and Richard L. Frock *

Division of Radiation and Cancer Biology, Department of Radiation Oncology, Stanford University School of Medicine, Stanford, CA 94305, USA

*To whom correspondence should be addressed. Tel: +1 650 497 6130; Fax: +1 650 723 7382; Email: frock@stanford.edu
Correspondence may also be addressed to Jinglong Wang. Email: jlwang90@stanford.edu

Abstract

Two DNA repair pathways, non-homologous end joining (NHEJ) and alternative end joining (A-EJ), are involved in V(D)J recombination and chromosome translocation. Previous studies reported distinct repair mechanisms for chromosome translocation, with NHEJ involved in humans and A-EJ in mice predominantly. NHEJ depends on DNA-PKcs, a critical partner in synapsis formation and downstream component activation. While DNA-PKcs inhibition promotes chromosome translocations harboring microhomologies in mice, its synonymous effect in humans is not known. We find partial DNA-PKcs inhibition in human cells leads to increased translocations and the continued involvement of a dampened NHEJ. In contrast, complete DNA-PKcs inhibition substantially increased microhomology-mediated end joining (MMEJ), thus bridging the two different translocation mechanisms between human and mice. Similar to a previous study on Ku70 deletion, DNA-PKcs deletion in G1/G0-phase mouse progenitor B cell lines, significantly impairs V(D)J recombination and generated higher rates of translocations as a consequence of dysregulated coding and signal end joining. Genetic DNA-PKcs inhibition suppresses NHEJ entirely, with repair phenotypically resembling Ku70-deficient A-EJ. In contrast, we find DNA-PKcs necessary in generating the near-exclusive MMEJ associated with Lig4 deficiency. Our study underscores DNA-PKcs in suppressing illegitimate chromosome rearrangement while also contributing to MMEJ in both species.

Graphical abstract

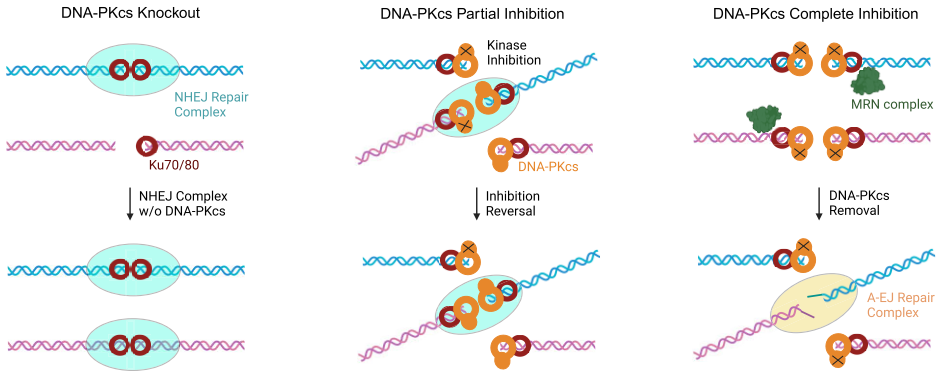

Introduction

The catalytic subunit of DNA-dependent protein kinase, DNA-PKcs, is a large protein (~460 kDa) present in vertebrates, and orthologs of this protein exist in a wide range of organisms including invertebrates, fungi, plants, and protists (1). DNA-PKcs forms a DNA-PK holoenzyme complex by binding with Ku70/80 and serves primarily in non-homologous end joining (NHEJ)-mediated repair of DNA double-stranded breaks (DSBs) (2–4). DNA-PK brings DNA ends together, forming long-range, short-lived synapsis. In the presence of X-Ray Repair Cross Complementing 4 (XRCC4), XRCC4-like factor (XLF), DNA ligase 4 (Lig4) and with or without Paralog of XRCC4 and XLF (PAXX), a short-range, long-lived mature synapsis is achieved (5,6) Structural studies further show that DNA-PK dimerizes and bends the broken DNA ends at an angle of approximately 90 degrees (7) and is present in the NHEJ supercomplex (8,9). However, an alternative NHEJ assembly is possible in the absence of DNA-PKcs (10). In addition, DNA-PKcs also initiates the DNA damage response by phosphorylating histone H2AX (11–13). Thus, we ask if DNA-PKcs functions as a hierarchical regulator that facilitates DSB repair in a timely manner to prevent DSB end uncoupling and illegitimate chromosome rearrangements (14–16).

Inhibition of DNA-PKcs in mouse cells increases the likelihood of broken ends from different chromosomes to co-localize, which is thought to increase chromosome translocation (17). In the context of murine immunoglobulin

Received: July 11, 2023. **Revised:** February 9, 2024. **Editorial Decision:** February 12, 2024. **Accepted:** February 14, 2024

heavy chain class-switch recombination, DNA-PKcs suppresses translocation to other genomic loci (18,19). However, the mechanisms of chromosomal translocation differ between mouse and human cells. In mice, alternative end joining (A-EJ) mechanisms predominantly form chromosome translocations, characterized in cycling cells by increased microhomology-mediated end joining (MMEJ); (20,21) notably, MMEJ does not wholly represent A-EJ and small microhomologies can be used for NHEJ. In contrast, NHEJ is primarily responsible for chromosome translocation in human cells (22). It remains unclear how DNA-PKcs affects the chromosome translocation rate in human cells.

Unlike chromosome translocation, V(D)J recombination is a physiological and highly orchestrated chromosome rearrangement process that occurs within antigen receptor loci of developing B and T lymphocytes. This multi-step process begins with (i) acquisition of compatible recombination signal sequence (RSS) pairs regulated by cohesion complexes and chromatin loops; (23) this is followed by (ii) RAG1/2 (RAG)-mediated DSB generation at each RSS/gene segment interface, resulting in a pair of hairpin sealed coding ends and blunt signal ends, held in a postcleavage synaptic complex, where (iii) NHEJ accesses and joins like ends to each other. Removal of the hairpin structure relies on the DNA-PKcs-dependent enzyme Artemis (24), highlighting the importance of DNA-PKcs in coding-coding joining. In mice, ablation of DNA-PKcs results in a massive failure of coding end joining, while signal end joining is partially affected, (25–27) due to redundant functions with ATM (28). However, the comprehensive impact of DNA-PKcs depletion on coding-coding, signal-signal, and illegitimate chromosome rearrangements (i.e. coding-signal joints, translocations etc.) has not been fully evaluated.

Therefore, we systematically investigated DNA-PKcs functions in suppressing illegitimate chromosome rearrangements, and to what extent A-EJ contributes to that process by employing the Linear Amplification Mediated High-Throughput repertoire, rejoin and Genome-wide Translocation Sequencing (LAM-HTGTS) methodologies (29–34). In both human Cas9- and mouse RAG-mediated DSB cell lines, we find that incomplete chemical inhibition of DNA-PKcs leads to increased chromosome translocation of blunt ended DSBs that are repaired by NHEJ, whereas complete genetic inhibition suppresses NHEJ-mediated translocations and increases MMEJ-mediated translocations, manifested most strikingly in cycling cells. DNA-PKcs deficiency can still form NHEJ-mediated translocations of blunt ends, but hairpin sealed ends, in the context of V(D)J recombination, are transitioned into a phenotypic *Ku70*$^{-/-}$ A-EJ mechanism for repair. However, unlike *Ku70*$^{-/-}$, DNA-PKcs deficiency does not restore the poor repair efficiency of *Lig4*$^{-/-}$ in non-cycling cells but does reduce their range of resected joints and converts their near-exclusive MMEJ activity into a more direct-dominant *Ku70*$^{-/-}$ junction structure pattern. These findings suggest that DNA-PKcs kinase activity is a crucial step to suppressing chromosome translocations and proceeding to complete repair by NHEJ that would otherwise be committed to repair involving MMEJ. They also suggest DNA-PKcs is not a major roadblock to A-EJ, but that it contributes to a Lig4-independent end joining pathway that engages DNA end resection and microhomology (MH) on protected ends with prolonged lack of repair.

Materials and methods

Plasmids preparation

The human Bcl2 gene (CDS) was cloned into a pLenti-puro vector to generate lentivirus. The Lenti-iCas9-Neo vector containing the Flag-iCas9-P2A-GFP cassette for Cas9 expression in K562 cells was obtained as a gift from Qin Yan (Addgene plasmid #85400) (35). For Cas9 expression in HEK293T cells, the neomycin-resistant gene of Lenti-iCas9-Neo was replaced with a blasticidin-resistant gene, resulting in the Lenti-iCas9-Blast vector. The CRISPR-Cas9 Guide RNA expression vector pMCB320 (Addgene #89359), (36) and the pMCB320-ACOC library (Addgene #101926), (37) bearing a mCherry reporter were obtained as gifts from Michael Bassik. The pMCB320 vector was used to clone guide RNAs targeting RAG1D, RAG1L and HBB sites, resulting in pMCB320-RAG1D, pMCB320-RAG1L and pMCB320-HBB, respectively.

Cell lines modification

The human immortalized myelogenous leukemia cell line, K562, derived from a CML patient (ATCC #CCL-243), was used in this study. K562-*Bcl2* cells were generated by transducing K562 cells with lentivirus bearing human Bcl2. K562-*PKcs*$^{-/-}$ cells were generated by introducing a DNA-PKcs exon-77 deletion using CRISPR-Cas9 in K562-*Bcl2* cells and verified by PCR, sanger sequencing and western blot (see the main text). K562-*iCas9* cells were generated by transducing K562 cells with lentivirus bearing iCas9-Neo. The K562 cell line and its modified versions were cultured at 37°C and 5% CO_2 in RPMI-1640 medium supplemented with 10% (vol/vol) fetal bovine serum (FBS), 50 U/ml penicillin/streptomycin/2 mM L-glutamine (Gemini Bio-Products, # 400-110), 1 × MEM-NEAA (Lonza, #13-114E), 1 mM sodium pyruvate (Cytiva, #SH30239.01), 50 μM 2-mercaptoethanol (Sigma-Aldrich, #M6250-100ML), and 20 mM HEPES (pH 7.4, Cytiva, #SH30237.01). K562-*Bcl2* and K562-*PKcs*$^{-/-}$ cells were selected with 5 μg/ml puromycin (Sigma-Aldrich, #P8833-100MG), and K562-*iCas9* cells were selected with 200 μg/ml G418 (BioVision, #2864-20). Doxycycline (2 μg/ml, Sigma-Aldrich, #D9891-10G) was added only when Cas9 expression was required. Doxycycline-treated cells were not used for cell line preservation.

The human embryonic kidney cell line, HEK293T, is an SV40 Large T antigen transformed derivative HEK293 epithelial cell line (ATCC #CRL-3216) was used in this study. HEK293T-*iCas9* cells were generated by transducing HEK293T cells with lentivirus containing iCas9-Blast. HEK293T and HEK293T-*iCas9* cells were cultured at 37°C and 5% CO_2 in DMEM supplemented with 10% (vol/vol) FCS, 50 U/ml penicillin/streptomycin, 2 mM L-glutamine, 1 × MEM-NEAA, 1 mM sodium pyruvate, 50 μM 2-mercaptoethanol, and 20 mM HEPES (pH 7.4). HEK293T-iCas9 cells were selected with 10 μg/ml blasticidin. Doxycycline (2 μg/ml) was added only when Cas9 expression was required. Doxycycline-treated cells were not used for cell line preservation.

The human colorectal carcinoma cell line, HCT116, with various DNA-PKcs gene editing including DNA-PKcs$^{+/-}$, DNA-PKcs$^{-/-}$ and DNA-PKcs$^{KD/-}$ were generated and verified as previously described (38). The DNA-PKcs-modified HCT116 cell lines were cultured at 37°C and 5% CO2 in

Hyclone α-minimum Eagle's medium supplemented with 5% newborn calf serum, 5% fetal bovine serum (Sigma), and 1 × penicillin/streptomycin (Gibco).

Mouse Abelson kinase-transformed progenitor B cell (*v-Abl)* lines including wild-type (*WT*), *Ligase 4*$^{-/-}$ (*Lig4*$^{-/-}$), *Ku70*$^{-/-}$, and *Lig4*$^{-/-}$*Ku70*$^{-/-}$ cells were reported in our previous study (clone A) (29). To generate new cell lines, DNA-PKcs was deleted using CRISPR/Cas9 in *WT* and *Lig4*$^{-/-}$ cells, resulting in cell lines *DNA-PKcs*$^{-/-}$ (#1/2) and *Lig4*$^{-/-}$*PKcs*$^{-/-}$ (#1/2), respectively. Confirmation of these cell lines was performed by genotyping using the primers listed in Supplementary Table S1. All *v-Abl* cells were cultured at 37°C and 5% CO_2 in RPMI-1640 medium supplemented with 10% (vol/vol) FBS, 50 U/ml penicillin/streptomycin/2 mM L-glutamine, 1 × MEM-NEAA, 1 mM sodium pyruvate, 50 μM 2-mercaptoethanol and 20 mM HEPES (pH 7.4). To induce V(D)J recombination, *v-Abl* cells were seeded at a concentration of 1 million cells/ml and supplemented with 3 μM STI-571 (TCI Chemicals, #I0936-100MG) for 4 days. Cells treated with STI-571 were not used for cell line preservation.

Mouse DNA-PKcs catalytically dead *v-Abl* cell lines, *DNA-PKcs*$^{KD/KD}$ #C1, #C3 and #C3-1 were generated and verified as previously reported (39). The cell culture conditions were the same as above for *v-Abl* cells except the base media DMEM.

Lentivirus production

Lentivirus was generated using the 2nd generation lentivirus packaging system. The transfer plasmid containing the gene or guide RNA of interest, the packaging plasmid psPAX2, and the envelope-expressing plasmid pMD2.G were mixed at a 4:3:1 mass ratio, which corresponded to 2, 1.5 and 0.5 μg, respectively, in 120 μl of opti-MEM (Fisher Scientific #31-985-070). To this mixture, 5 μl of the p3000 reagent was added and mixed thoroughly. In a separate tube, 5 μl of lipofectamine 3000 (Thermo Scientific, #L3000015) was mixed with 120 μl of opti-MEM and mixed thoroughly. The DNA mixture was then added drop by drop to the lipofectamine mixture, mixed well, and left at room temperature for 15 min.

Next, the lipofectamine-DNA mixture was added to one well of HEK293T cells cultured in a 6-well plate and maintained in culture media for an additional two days. The media containing lentivirus was collected on day 2, and 2.5 ml of fresh media was added to the cells, which were maintained for one more day. The media was then collected again to obtain more lentivirus. The lentivirus titration was recommended to be performed in the targeting cell lines rather than in HEK293T cells alone.

Immunoblotting

The samples, including K562-*WT*, K562-*Bcl2*, K562-*PKcs*$^{-/-}$ and K562-*iCas9*, were collected at a concentration of 5 million cells and resuspended in 200 μl of RS buffer (150 mM NaCl, 10 mM Tris pH 7.5). Cell lysis was performed by adding 200 μl of 2× Laemmli buffer (4% SDS, 5% 2-mercaptoethanol, 20% glycerol, 0.004% bromophenol blue, 125 mM Tris pH 6.8) and incubating at 95°C for 10 minutes. The lysate samples were loaded directly onto a 4–15% TGX precast SDS-PAGE gel (Bio-Rad, #4561084). Protein transfer onto a nitrocellulose membrane was carried out using the Turbo™ Transfer System (Bio-Rad, #1704150) and the corresponding transfer kit (Bio-Rad, #1704271). Immunoblotting was performed using the following antibodies: anti-Bcl2 (1:2000, Novus Biologicals #NB100-56098), anti-Flag (1:2000, Cell Signaling Technology #12793S), anti-DNA-PK (1:4000, Origene #TA314389), anti-Rabbit-IgG (1:2000, Thermo Scientific #G-21234), and anti-actin (1:4000, Santa Cruz Biotechnology #SC-47778). Protein band detection was accomplished using an HRP substrate (Advansta #K-12042-D10) and visualized under a chemiluminescent imaging system, ChemiDoc (See Supplementary Figure S1A, D). The Cas9 expression level in HEK293T-iCas9 cells was detected using the same approach (See Supplementary Figure S1G). The phosphorylation state of DNA-PKcs S2056 (PKcs p^{S2056}) was detected using the corresponding antibody (Thermo Scientific #PA5-121294) in similar manner, except phosphatase inhibitors were added in cell lysis. After detection of PKcs p^{S2056}, its antibody was removed by stripping buffer (Takara Bio #T7135A) and re-blotted by PKcs antibody to quantify the total amount of DNA-PKcs (see Supplementary Figure S2I–L).

Quality control by flow cytometry

Cell cycle analysis

The cell cycles of K562-*Bcl2* cells, with or without Palbociclib, DPKi #1/2, and ATMi, were assessed based on DNA replication activity. Briefly, 50 μM EdU (Cayman #20518) was added to each condition and incubated for 30 minutes. The EdU-treated cells were fixed with 2% formaldehyde (EMS #15710) for 15 min at room temperature, permeabilized with 0.5% TritonX-100 for 15 min at room temperature and subjected to click labeling reaction using AFDye 488 Azide (Click Chemistry Tools, #1314). The AFDye 488-labeled cells were analyzed by flow cytometry using the FITC channel.

Plasmid delivery into K562 and HCT116 cell lines

For delivering plasmids into K562-*Bcl2* and K562-*iCas9* cells, the 4D-nucleofector system (Lonza, Core plus X unit) and SF Cell Line 4D X Kit (Lonza, #V4XC-2024) were employed. Four million K562-*Bcl2* cells were nucleofected with 5 μg pX330-RAG1D, 5 μg pX330-RAG1L and 0.5 μg pMAX-GFP. The cells were then cultured for 2 days. Nucleofection efficiency was determined by measuring GFP expression from the pMAX-GFP vector using the FITC channel of flow cytometry. Similarly, four million K562-*iCas9* cells were nucleofected with 5 μg pMCB320-ACOC plus 5 μg pMCB320-RAG1L or 5 μg pMCB320-ACOC plus 5 μg pMCB320-HBB. The cells were cultured for two days, and nucleofection efficiency was evaluated by detecting mCherry expression from the pMCB320 vector using the Cy5 laser channel of flow cytometry. The expression level of Cas9 upon Doxycycline induction was correlated with GFP expression detected by the FITC channel. Plasmids including pX330-RAG1D, pX330-RAG1L and pMAX-GFP were delivered into HCT116 cells same as K562-*Bcl2* cells but using the SE Cell Line 4D-Nucleofector™ X Kit (V4XR-1024), and nucleofection efficiency was evaluated similarly as above.

Plasmid transfection into HEK293T-*iCas9* cells

HEK293T-*iCas9* cells were transduced in 6-well plates with 2.5 μg pMCB320-RAG1D and 2.5 μg pMCB320-RAG1L or with 4 μg pMCB320-ACOC and 1 μg pMCB320-RAG1L, using the lipofectamine 3000 kit. The cells were maintained in D10 media, with or without DPKi #1/2. Transfection

efficiency was determined by measuring mCherry expression from the pMCB320 vector using the Cy5 laser channel of flow cytometry. The expression level of Cas9 upon Doxycycline induction was correlated with GFP expression detected by the FITC channel.

LAM-HTGTS library preparation

HTGTS library preparation was performed as previously described (31) with some modifications. For K562-*Bcl2*, K562-*iCas9*, HEK293T-*iCas9* and HCT116 libraries, 5 μg of genomic DNA from each treatment condition was sheared using a bioruptor sonication device (Diagenode) in low mode for two cycles (30s on + 60s off) at 4°C, resulting in fragments ranging from 200 bp to 2 kb. The sheared fragments were subjected to linear amplification (LAM)-PCR using biotin-labeled primers, including Bio-RAG1L and Bio-HBB proximal to the RAG1L and HBB cleaved sites (baits), respectively. The LAM-PCR products were enriched using streptavidin-coated magnetic beads, followed by adapter ligation. Unligated adapters were removed, and the ligated products were subjected to nested-PCR using a common primer (AP2I7-novo) matching the adapter sequence and another barcoded I5 primer that matches the region between the bait-site and the biotin-labeled primer. The DNA from the nested-PCR was purified using a Gel-extraction kit (Qiagen #28706). Subsequently, tagged PCR was performed using primers P7I7 and P5I5, which match the primers used in the nested-PCR. The PCR products were purified by 1% agarose gel electrophoresis, and DNA products with a length of 500 bp to 1 kb were excised and extracted using a Gel-extraction kit. The tagged DNA libraries were subjected to bioanalyzer analysis for quality control and sequencing using the Illumina NovaSeq-PE150. Please refer to Supplementary Table S2 for the oligos used.

The HTGTS library of mouse *v-Abl* cells was prepared using a similar approach, with the following modifications: (i) 2 μg of genomic DNA/sample was used for each library; (ii) barcoded AP2I7-novo primers were used, and the nested-PCR products from each of the 12 libraries were pooled and tagged ensemble in tagged PCR; (iii) Jκ1, Jκ2, Jκ4 and Jκ5 coding and signal end-specific biotin-labeled primers, as well as nested I5 primers, were used. Please refer to Supplementary Table S2 for the oligos used.

Data analyses

LAM-HTGTS data analysis was performed following previously reported methods (29,31). Briefly, sequencing reads from Illumina NovaSeq PE150 were de-multiplexed based on the inner barcodes and the sequence between the bait site and the nested PCR I5 primers using the fastq-multx tool from ea-utils. The adapter sequences were trimmed using the SeqPrep utility. The demultiplexing and trimming functions were integrated into a script called TranslocPreprocess.pl. Subsequently, the reads were normalized using Seqtk and mapped to the hg19 or mm9 reference genome using TranslocWrapper.pl to identify chromosome translocations or V-J recombination events, generating result tlx files. Junctions that aligned to the bait region were not shown in the result tlx files and were extracted separately using a script called JoinT.R, resulting in final tlx files containing translocations and rejoin events. JoinT.R was omitted for V-J recombination analysis. Junction duplications were retained as described previously (29,33).

Result and final tlx files were converted into bedgraph files using tlx2bed.py, (31) which were then visualized and plotted using IGV (integrative genomics viewer). Junctions in regions of interest from the result and final tlx files were extracted using tlxbedintersect.py, which relied on two other scripts, tlx2BED.pl and pullTLXFromBED.pl (31). The regions of interest varied depending on the specific paradigm. For Vκ-Jκ recombination in *v-Abl* cells, the regions of interest were the RAG1/2 cleavage sites of Vκ genes, with a flanking 200 bp window (± 200). In the case of twinned Cas9-cleaved K562-*Bcl2*, the region of interest was the RAG1D 'prey' locus. In the genome-wide DSBs generated by ACOC libraries in K562-*iCas9* and HEK293T-*iCas9* cells, the final tlx files were converted into bed files using tlx2BED-MACS.pl and evaluated using the peak caller MACS2, resulting in a peaks.xls file that contained the junction peaks and their significance. The peak regions in control and experimental conditions were combined together and used as regions of interest.

Junctions were plotted using TranslocPlot.R, (14) which provided visualization of the chromosomes and the locations of junctions across the genome. These commands could be used for plotting junctions across the entire genome or within a specific region on a given chromosome. Circos plots were generated using the circos package, combining the binfile.txt from the junction plot and the count.bed from tlxbedintersect.py. The result and final tlx files could also be utilized for repair pathway and resection analyses. JctStructure.R was employed to determine the repair patterns, including microhomology, direct repair, and insertion. The degree of DSB end resection, indicated by the distribution of junctions near the DSB break site, was quantified using ResectionRSS.R.

All essential HTGTS-related codes are in the following links:

https://github.com/JinglongSoM/LAM-HTGTS
https://github.com/marielebouteiller/JoinT-seq
http://robinmeyers.github.io/transloc_pipeline/thedocs.html
https://expressionanalysis.github.io/ea-utils/
https://github.com/jstjohn/SeqPrep
https://github.com/lh3/seqtk
https://software.broadinstitute.org/software/igv/
https://pypi.org/project/MACS2/

The data obtained from western blot and flow cytometry experiments were analyzed using ImageJ (NIH) and FlowJo (FlowJo, LLC), respectively.

Statistical analysis

All data were presented as mean ± SEM if not otherwise indicated. Analyses of differences were determined using one-way ANOVA plus Dunnett's multiple comparisons, or Student's *t*-test (unpaired Student's t-test for the data obtained in same batch and ratio paired Student's *t*-test for the data obtained in different batches). Statistical analyses were performed using GraphPad Prism (GraphPad Software, Inc.). Where necessary, linked experimental sets were displayed to discern batch effects. All P values presented were two-tailed, and $P < 0.05$ was considered statistically significant.

Results

The significance of DNA-PKcs in physiological DNA damage repair has led to the development of inhibitors for can-

cer treatment (40–44). For this study, we chose two well-established inhibitors, Nu7441 (DPKi #1 at 500nM) and Nu7026 (DPKi #2 at 20μM). As ATM has been extensively characterized in suppressing chromosome translocation, (45) we also included Ku-60019, a specific ATM inhibitor (ATMi at 10μM), as a control (46). Inhibitor concentrations were determined by the minimal amount that promoted chromosome translocations in pilot experiments (Supplementary Table S3). We used the CRISPR-Cas9 system in K562 and HEK293T cell lines (Supplementary Figure S1A-S1I) (see methods). To minimize cell death by nucleofection, we introduced the anti-apoptosis gene Bcl2 into K562 cells, resulting in the generation of a novel cell line, K562-*Bcl2*. Western blot analysis confirmed significantly higher expression levels of Bcl2 in K562-*Bcl2* cells compared to the parental cell line, K562-*WT* (Supplementary Figure S1A), and the efficiency of nucleofection was assessed by co-nucleofecting a GFP vector along with CRISPR-Cas9 (Supplementary Figure S1B, C). We separately generated inducible Cas9-expressing cell lines, K562-*iCas9* and HEK293T-*iCas9*, and confirmed Cas9 expression upon induction with Doxycycline using western blot analysis (Supplementary Figure S1D, G). Guide RNA (gRNA) pools were delivered (37) with high level gRNA expression (Supplementary Figure S1E, F, H, I).

We first confirmed the effect of these inhibitors did not drastically affect cell cycle progression (Supplementary Figure S2A–D) and then next investigated whether the treatment with these inhibitors would have a similar affect under G1/G0 arrest using the cdk4/6 inhibitor, Palbociclib (47,48). G1/G0 arrest was achieved with 50μM Palbociclib in K562 cells, and the inclusion of DPKi #1, DPKi #2, or ATMi did not interfere with the cell cycle arrest induced by Palbociclib (Supplementary Figure S2E–H). To confirm the efficacy of the DNA-PKcs inhibitors, we performed immunoblotting to detect the total level of DNA-PKcs and its auto-phosphorylated form at Ser2056 (pS2056). We observed a marginal decrease in total DNA-PKcs levels, while the DNA-PKcs autophosphorylation at Ser2056 was significantly reduced upon treatment with DPKi #1 and DPKi #2 in cycling K562-*Bcl2* cells (Supplementary Figure S2I, J), as well as in Palbociclib-treated cells (Supplementary Figure S2K, L). Based on these results, we conclude that DPKi #1 and DPKi #2 do not perturb the cell cycle in the context of our study.

Increased intrachromosomal translocation by partial DNA-PKcs inhibition

Using nucleofection in K562-*Bcl2* cells, we employed a pair of Cas9:gRNAs in the RAG1 locus (RAG1D and RAG1L) on chromosome 11 to generate DSBs using the RAG1L cleavage site as the bait, enabling the detection of junctions arising from single (rejoined) or dual (translocated to RAG1D) Cas9-generated DSBs via HTGTS-JoinT-seq (29) (Figure 1A), which for the latter would include deletions and inversions based on chromosome orientation. Repair patterns of these DSBs are consistent with the generation of predominantly blunt ends (49). For these experiments, we derived a translocation rate (TL) by normalizing against the number of rejoin events (Figure 1A). In cycling K562-*Bcl2* cells, we generated hundreds of thousands of junctions (Supplementary Tables S4 and S5) and observed an increased number of translocations in the presence of DNA-PKcs inhibitors, DPKi #1 and DPKi #2, compared to the DMSO control that was accompanied by a decrease in the number of rejoins (Figure 1A). Conversely, ATMi treatment resulted in a slight decrease in the number of translocations but with a significant drop in rejoins that was on average 50% greater than with DPKi treatments (Figure 1A). Consequently, all inhibitors led to an elevated translocation rate, with a two-fold increase in ATMi and DPKi #1, and a three-fold increase in DPKi #2, compared to the DMSO control (Figure 1B). Previous work demonstrated that non-homologous end joining (NHEJ) is responsible for chromosome translocation in human cells (22). To investigate if the observed increase in chromosome translocation from inhibited DNA damage signaling was due to A-EJ, we analyzed junction structures of the resulting translocations. Unexpectedly, joints remained predominately direct (Figure 1C), suggestive of continued utilization of NHEJ.

We next investigated whether DNA-PKcs inhibition affected chromosome translocation in G1/G0-arrested K562-*Bcl2* cells. Under these conditions we accumulated ∼2-fold fewer total junctions compared to the cycling counterparts (Supplementary Tables S4 and S5). Similar to our cycling experiments (Figure 1A–C), DPKi #1 and DPKi #2 increased the number of translocations and reduced the number of rejoins compared to the DMSO control, while ATMi decreased both the number of translocations and rejoins (Figure 2A). Consequently, the translocation rate was significantly higher for DPKi #1 and DPKi #2 while ATMi showed a slight upward trend compared to the DMSO control (Figure 2B). Further analysis of translocation junction structures did not reveal any changes relative to the control, which were direct and indicative of NHEJ (Figure 2C).

From the above findings, chromosome translocations are mediated by NHEJ, regardless of the presence or absence of DNA-PKcs inhibitors; however, Ku70 deficiency in G1/G0-arrested *v-Abl* cells, (29) representing a robust A-EJ pathway that also leverages direct joining, may not be readily distinguished if DPKi effects favor this pathway over NHEJ. To test for this possibility, we inhibited two crucial components of A-EJ, poly(ADP-ribose) polymerase-1 (Parp1) (50,51) and polymerase theta (Polθ), (52) using Olaparib (Parpi at 10μM) (53) and Novobiocin (Polθi #1 at 100 μM) (54) in G1/G0-arrested K562-*Bcl2* cells, with or without the DNA-PKcs inhibitor DPKi #2. Here, DPKi #2 had the most pronounced effect, leading to an increase in translocations and a decrease in rejoins (Supplementary Figure S3A). Parpi and Polθi #1 slightly elevated both translocations and rejoins, irrespective of the presence or absence of DPKi #2. Consequently, we observed no significant change in the translocation rate with Parpi or Polθi #1 alone or when combined with DPKi #2 (Supplementary Figure S3B). Further analysis of the Cas9 translocation repair pattern did not reveal any significant changes (Supplementary Figure S3C).

To validate our findings in a different cell line, we performed similar experiments in HEK293T-*iCas9* cells, where the same pair of gRNAs were used (RAG1D and RAG1L) for targeted DSB generation upon doxycycline induction (see methods). We observed a similar increase in translocation events upon DNA-PKcs inhibition, with no alterations in translocation junction structures (Supplementary Figure S4A–C), and similar effects were observed upon ATMi treatment (Supplementary Figure S4D, E) (Supplementary Tables S4 and S5). Thus, we conclude that DNA-PKcs inhibition at the doses assayed promotes proximal chromosome translocation by NHEJ.

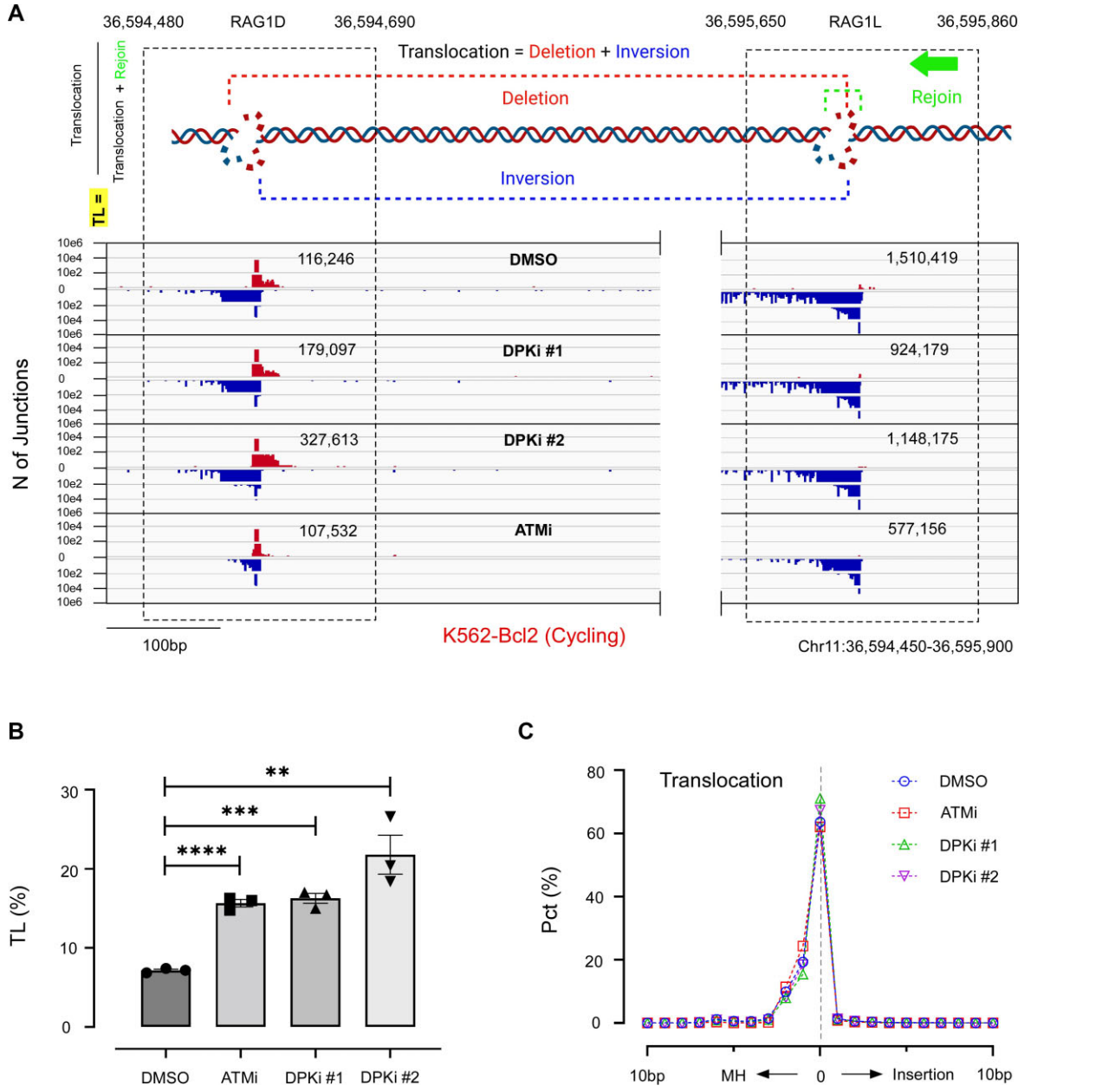

Figure 1. Increased NHEJ-mediated intrachromosomal translocations by partial DNA-PKcs inhibition in cycling K562-Bcl2 Cells. (**A**) Cas9:RAG1D 'prey' and Cas9:RAG1L 'bait' DSBs on chromosome 11 for high-throughput genome-wide translocation sequencing (HTGTS; green arrow). Three dominant types of repair junctions were formed: deletion (red dashed line), inversion (blue dashed line) and rejoin (green dashed line). Cas9:RAG1D translocation rate (TL): (deletions + inversions) / (rejoin + deletions + inversions). IGV plots display junction profiles of the RAG1D and RAG1L sites for DMSO, DPKi #1, DPKi #2 or ATMi conditions. (**B**) TL rates for the tested conditions: DMSO (7.15 ± 0.16%), ATMi (15.68 ± 0.47%), DPKi #1 (16.26 ± 0.62%), and DPKi #2 (21.79 ± 2.46%). Statistical significance between DMSO and inhibitors was assessed using unpaired *t*-test; $^{**}P < 0.01$; $^{***}P < 0.001$; $^{****}P = 0.0001$. (**C**) Percent Translocation junction structure distributions were categorized into bps of microhomology (MH), insertion, and direct repair ('0'). Experiments were from three biological replications, and error bars using standard error of the mean (SEM).

Partial DNA-PKcs inhibition promotes genome-wide translocations

We investigated whether the phenomenon observed with the Cas9:RAG1D prey site applies more broadly, by generating genome-wide double-strand breaks (DSBs) using a gRNA library, ACOC, which contains approximately 30,000 different gRNAs (37). These DSBs were introduced in G1/G0-arrested K562-*iCas9* cells while using the Cas9:RAG1L DSB as bait for JoinT-seq library preparation and recovered ∼200,000–300,000 total junctions per replication (Supplementary Tables S4 and S6). Considering recent findings highlighting the role of topologically associated domains (TADs) in DNA damage repair (55), we defined TAD boundaries based on CTCF and RAD21 chip-seq data (Supplementary Figure S5A) and evaluated junctions located beyond the RAG1 TAD. Quantification of these genome-wide translocations and bait DSB rejoins clearly indicate significantly more translocations and less rejoins for DPKi #1 and DPKi #2 conditions relative to DMSO control (Figure 3A). Applying a similar translocation (TL) rate measure but now for translocations exterior to the RAG1 TAD, exTAD-TL, was >2-fold higher in the DPKi #1 and DPKi #2 conditions compared to the DMSO control

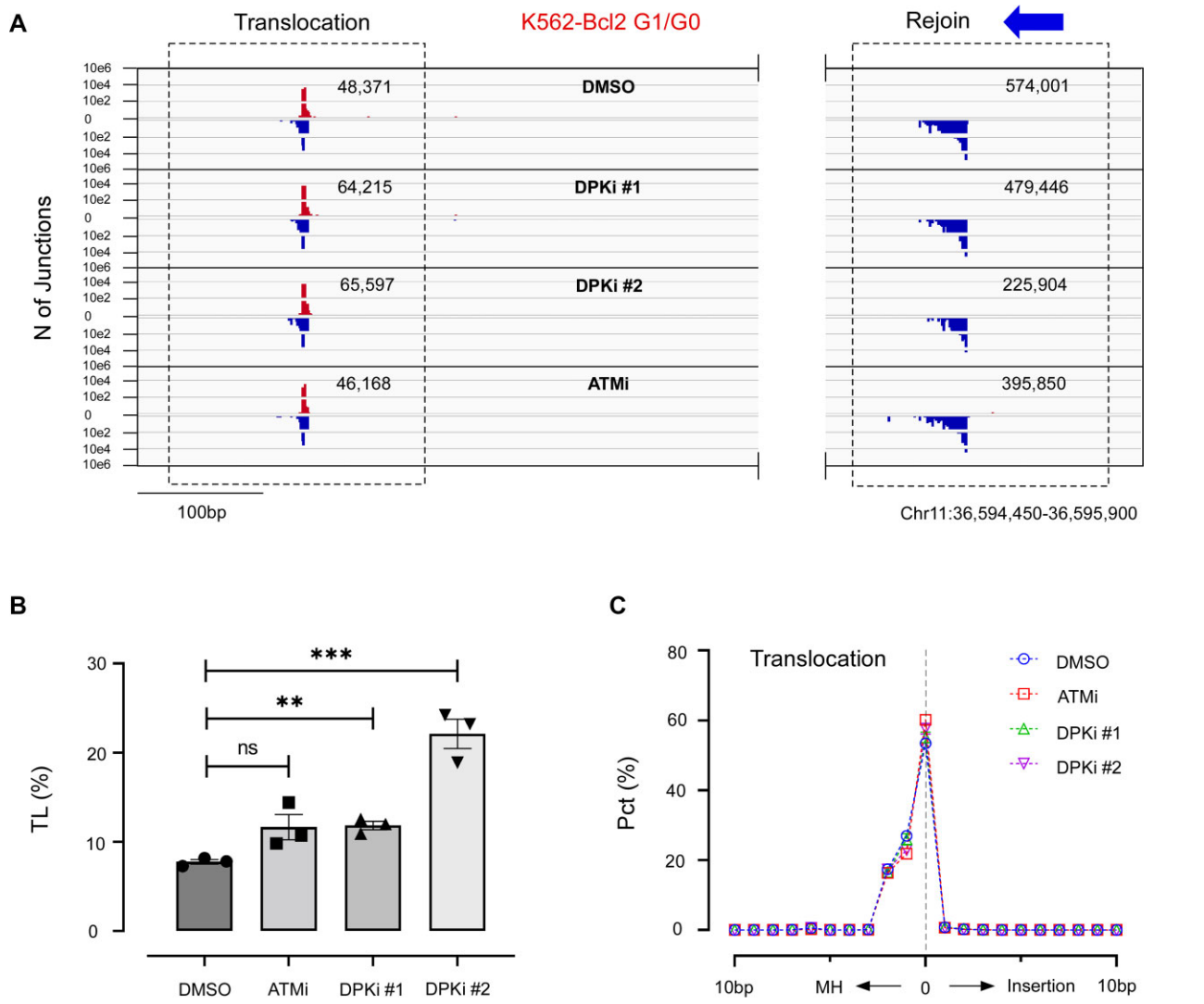

Figure 2. Partial DNA-PKcs inhibition promotes NHEJ-mediated intrachromosomal translocations in G1/G0-arrested K562-Bcl2 cells. (**A**) IGV junction profile plots of RAG1D and RAG1L sites in the presence of cdk4/6 inhibition (Palbociclib) and treated with DMSO, DPKi #1, DPKi #2 or ATMi. Blue arrow indicates the bait site. (**B**) TL rates for DMSO (7.78 ± 0.26%), ATMi (11.66 ± 1.41%), DPKi #1 (11.85 ± 0.47%) and DPKi #2 (22.12 ± 1.64%), evaluated by unpaired *t*-test; $^{**}P < 0.01$; $^{***}P < 0.001$; ns, not significant. (**C**) Translocation junction structure distributions; see Figure1 legend for details. Experiments were independently repeated three times, and SEM are provided.

(Figure 3B). Importantly, this more diverse collection of Cas9:gRNA-targeted chromosome translocations were still predominantly direct, indicative of NHEJ, and with no significant perturbation observed upon DPKi #1/2 treatment (Figure 3C). Genome-wide translocation analysis was also conducted in cycling HEK293T-*iCas9* cells, and consistent results were obtained (Supplementary Figure S6A; Supplementary Tables S4 and S6), including no significant changes in junction structure patterns (Supplementary Figure S6B, C).

To determine if the increased translocation upon DNA-PKcs inhibition was specific to the previous bait site, we employed a separate bait site in the HBB locus on chromosome 11 which was then subjected to the same ACOC gRNA library and assayed in G1/G0 arrested K562-*iCas9* cells (Supplementary Figure S7A; Supplementary Tables S4 and S6). The TAD domain encompassing the HBB locus was determined based on CTCF binding sites (Supplementary Figure S5B). Again, significantly increased exTAD-TL values were observed in DPKi #1 and DPKi #2 (Supplementary Figure S7B), while no changes were found in the repair patterns (Supplementary Figure S7C). These findings suggest the increased chromosome translocation induced by DNA-PKcs inhibitors is a general phenomenon.

Complete DNA-PKcs inhibition promotes MMEJ-mediated translocations

Although DPKi #1/2 inhibitors enhanced the translocation effect with no discernable change in junction structure patterns, autophosphorylation levels were not completely absent (Supplementary Figure S2I, J), indicating incomplete kinase inhibition. Thus, we retested DNA-PKcs inhibition with a 10-fold increased concentration of DPKi #1 (5μM) and included two more potent DNA-PKcs inhibitors, DPKi #3 (AZD7648, 10μM) (56,57) and DPKi #4 (M3814, 10μM) (56,58); in parallel to this experiment, we also tested the effect of a second Polθ inhibitor, ART558 (Polθi #2 at 10μM), (59) in combination with DPKi #2. In G1/G0 arrested K562-Bcl2 cells, Polθi #2 displayed no significant change in translocations alone or

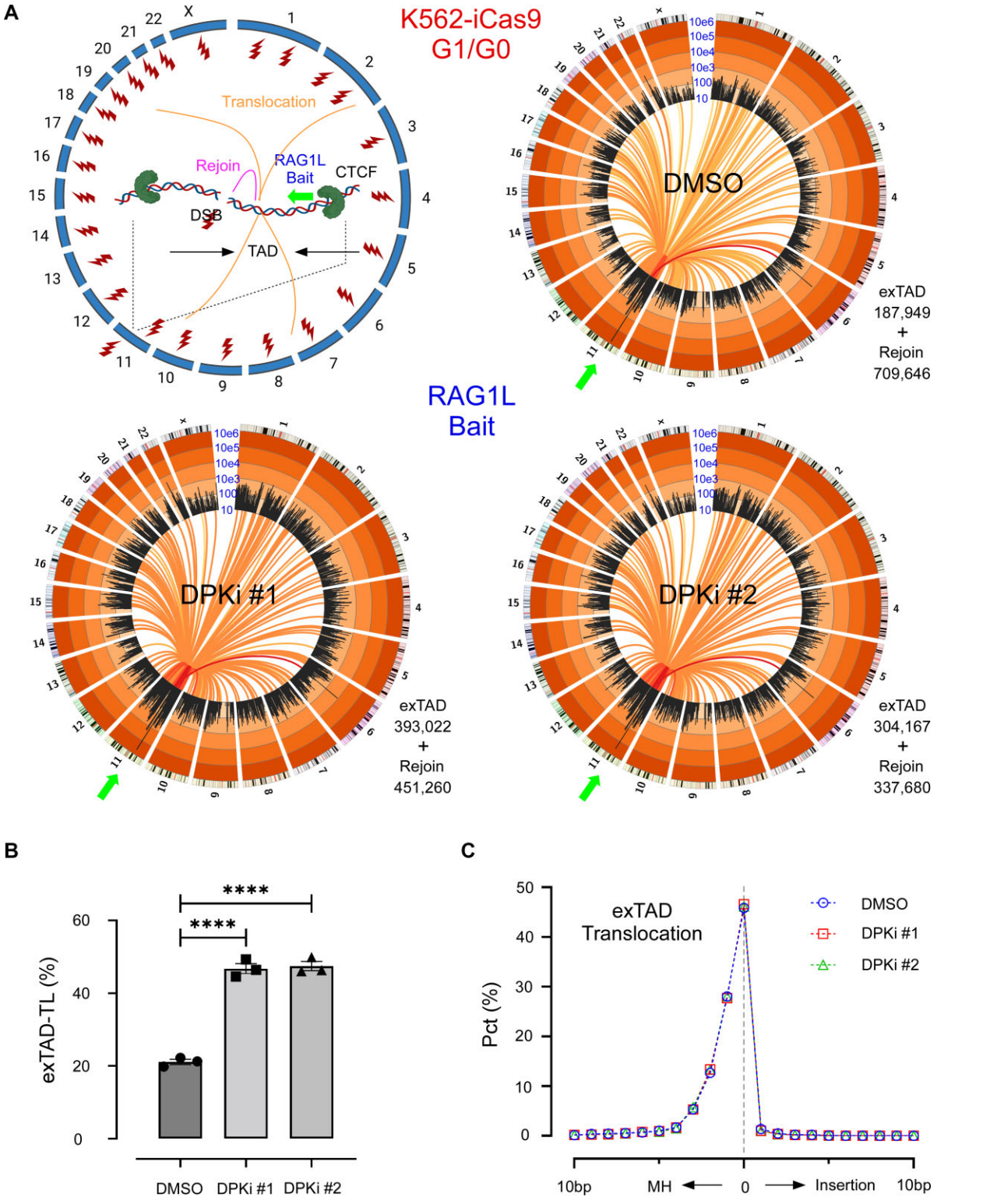

Figure 3. Partially inhibited DNA-PKcs promotes genome-wide translocations. (**A**) To generate double-strand breaks (DSBs), ∼30,000 ACOC library gRNAs (represented as red lightning bolts) were transfected in G1/G0-arrested K562-iCas9 cells with doxycycline induction of Cas9. The RAG1L gRNA was used as bait for HTGTS (green arrows). (Top left) Translocations and rejoins are depicted by orange and magenta lines, respectively. The bait site is flanked by convergently oriented CTCF binding sites, forming a Topology-Associated Domain (TAD, Chr11: 36585950–36644640). The genome-wide translocation profiles for DMSO, DPKi #1, and DPKi #2 conditions are shown as circos plots with junction frequencies reported within (Rejoin) or genome-wide (exTAD). Black bars indicate 5 Mb binned chromosome regions and their frequency is indicated on log scale. Yellow to red colored lines connect bait to prey hotspots with red being the most significant. (**B**) The TL rates measuring junctions outside the TAD region (exTAD) normalized to the number of rejoins within the TAD (exTAD-TL). The exTAD-TL changes between DMSO (21.10 ± 0.71%), DPKi #1 (46.76 ± 1.38%), and DPKi #2 (47.43 ± 1.24%) were evaluated by unpaired *t*-test. ****$P < 0.0001$. (**C**) Junction structure distributions for exTAD translocations; see Figure 1 legend for more details. Experiments were independently repeated three times, and SEM are provided.

with DPKi #2 and did not alter junction structure patterns (Figure 4A–C). The higher dose of DPKi#1 and the effect of DPKi #3 and #4 increased translocation rates, as expected (Figure 4A), however, the dosing efficacy of DPKi #1, 3 and 4 also significantly decreased translocation frequency (Figure 4B), indicating a substantial block in NHEJ. It is notable that no obvious cell death was detected within two-day experiment window. Junction structure patterns from interchromosomal translocations revealed a slight increase in MMEJ for DPKi #3/4 conditions (Figure 4C), which were the most affected. Importantly, MMEJ utilization became strikingly near-exclusive when DPKi #3/4 were tested again under cycling conditions despite having significant reductions in translocation frequency (Figure 4D–F). We conclude a more robust chemical inhibition of DNA-PKcs kinase activity suppresses NHEJ-mediated repair and will ultimately transition to using MMEJ, particularly in cycling conditions.

We next wanted to contrast repair outcomes with DNA-PKcs deficiency by generating in K562-*Bcl2* cells a deletion in the kinase domain of DNA-PKcs (Δexon-77). Western analysis indicated the deletion generated a truncation at a markedly low level (Supplementary Figure S8A-S8B). While recovered total junctions with kinase domain deletion in G1/G0-phase were robust and averaged ∼83,000–108,000 (Supplementary Figure S8C), the translocation rate and junction structure patterns remained unchanged with DPKi #1 (0.5 μM) or DPKi #2 treatments (Supplementary Figure S8D-S8E). However, DNA-PKcs deficiency revealed increased MMEJ from the Cas9:RAG1D prey DSB, although the major peak still corresponded with direct repair; extended analysis to interchromosomal translocations also revealed a doubled increase in MH utilization (MH > 3 bp) in the PKcs$^{-/-}$ versus the parental line (Supplementary Figure S9A-S9B). Consequentially, we found Parpi, but not Polθi #2, reduced MMEJ and increased direct repair despite neither inhibitor affecting the translocation rate (Supplementary Figure S8F, G). Therefore, we conclude hypomorphic kinase truncation of DNA-PK promotes some MMEJ that involves Parp activity.

A prior report was not able to derive clonal lines of early exon DNA-PKcs deletions in HCT116 cells, (60) which was analogous to our efforts in K562 cells but was able to do so with late exon deletions. More recently, sets of full DNA-PKcs deletion (in or after exons coding for the C-terminal kinase domain) and DNA-PKcs catalytically dead point mutations were reported (38,61). We applied our dual Cas9:gRNA approach to cycling HCT116 *DNA-PKcs*$^{+/-}$, *DNA-PKcs*$^{-/-}$ and *DNA-PKcs*$^{KD/-}$ lines, (38) which harbor an exon-79 deletion or K3753R kinase dead (KD) point mutation in exon-79, to measure changes in repair outcomes. Western Analysis confirmed comparable levels of DNA-PKcs in the heterozygous and kinase dead cell lines and a complete absence of protein in the knockout (Figure 5A, B). We found that both the translocation frequency and the translocation rate were dramatically increased in *DNA-PKcs*$^{KD/-}$, but not *DNA-PKcs*$^{-/-}$ cells, compared to the parental *DNA-PKcs*$^{+/-}$ control (Figure 5C, D). Further junction structure analysis of Cas9 and interchromosomal translocations indicated increased MMEJ only in *DNA-PKcs*$^{KD/-}$ and not in *DNA-PKcs*$^{-/-}$ cells (Figure 5E, Supplementary Figure S9C, D). Collectively, we conclude genetic DNA-PKcs kinase inhibition, similar to robust chemical DNA-PKcs inhibition, enhances translocations that are repaired more frequently by MMEJ.

End joining pathway choice on V(D)J recombination is determined by DNA-PKcs protein and kinase status

With the above observations in mind for human cells, we wanted to discern NHEJ/A-EJ outcomes from DNA-PKcs inhibition versus deficiency in mouse *v-Abl* pro-B cell lines which undergo G1/G0 arrest and V(D)J recombination of hairpin sealed coding ends, and separately for blunt signal ends. We focused analysis on the Igκ light chain locus Vκ-Jκ pairing and cleavage of >100 functional Vκ-gene segments with four Jκ-gene segments by the RAG endonuclease; we used HTGTS-V(D)J-seq employing all functional Jκ coding end baits (Jκ1CE, Jκ2CE, Jκ4CE, and Jκ5CE) to assess DNA-PKcs perturbations (DPKi #2 (20 μM) or DNA-PKcs exon 1 knockouts – *DNA-PKcs*$^{-/-}$ #1 and *DNA-PKcs*$^{-/-}$ #2) (Supplementary Figure S10A) relative to wild-type (*WT*; NHEJ) and *Ku70*$^{-/-}$ (A-EJ) backgrounds (29). For reference, the Jκ1 coding end bait in WT cells robustly forms coding joins (Figure 6A).

We measured the Vκ-Jκ recombination efficiency (V-J Eff) and interchromosomal translocation fraction (TL) by normalizing Vκ region junctions against total reads and interchromosomal junctions against the total junctions recovered, respectively (Supplementary Table S7). The recombination efficiency was decreased by >10-fold for *DNA-PKcs*$^{-/-}$ #1/2 and *Ku70*$^{-/-}$ cells compared to the *WT* control; *WT* + DPKi #2 cells were moderately depressed (Figure 6B), owing to the incomplete kinase inhibition. A corresponding reverse trend was found for the translocation fraction where DNA-PKcs deletion and inhibition increased the interchromosomal translocation rate (Figure 6C), suggestive of the utilization of A-EJ in the absence of DNA-PKcs. Junctions enriched around the ± 10 bp coding/signal RAG incision sites of functional Vκ gene segment regions were quantified; unlike *WT* and *WT* + DPKi, which were not resected beyond 10 bp, DNA-PKcs deletion reduced the enrichment by ∼70%, similar to *Ku70*$^{-/-}$ (Figure 6D–E). Junction structures of Vκ-Jκ recombinants from JκCE baits revealed some distinguishing patterns. First, although common to all comparisons were the notable peak of direct joints, *WT* and *WT* + DPKi cells displayed the most (∼20%) insertions (<4 bp), consistent with NHEJ utilization; this was followed by *DNA-PKcs*$^{-/-}$ #1/2 clones with an intermediate insertion fraction, while *Ku70*$^{-/-}$ possessed very few insertions. Second, while *WT* and *WT* + DPKi cells displayed fewer short MHs (1–3 bps) than *Ku70*$^{-/-}$ cells, *DNA-PKcs*$^{-/-}$ #1/2 clones consistently tracked along the same *Ku70*$^{-/-}$ MH enrichment path for all baits (Figure 6F and Supplementary Figure S10B-S10D). Collectively, the coding end data suggest the absence, but not the inhibition, of DNA-PKcs has dramatic effects on V(D)J recombination and chromosome translocation, and the residual joining in the absence of DNA-PKcs harbors partially overlapping features of NHEJ and A-EJ.

Although signal-signal joining does not require DNA-PKcs, (62) the consequence of promoting A-EJ from JκCE baits suggests a reciprocal possibility for signal end baits. Thus, we utilized corresponding Jκ signal ends (Jκ1SE, Jκ2SE, Jκ4SE and Jκ5SE) using the above analysis parameters for evaluation (Figure 6G and Supplementary Figure S11A–F). Similar to CE baits, *WT* + DPKi #2 had a moderate decrease in recombination efficiency, whereas efficiency was reduced by ∼5-fold in the *DNA-PKcs*$^{-/-}$ #1/2 and *Ku70*$^{-/-}$ clones

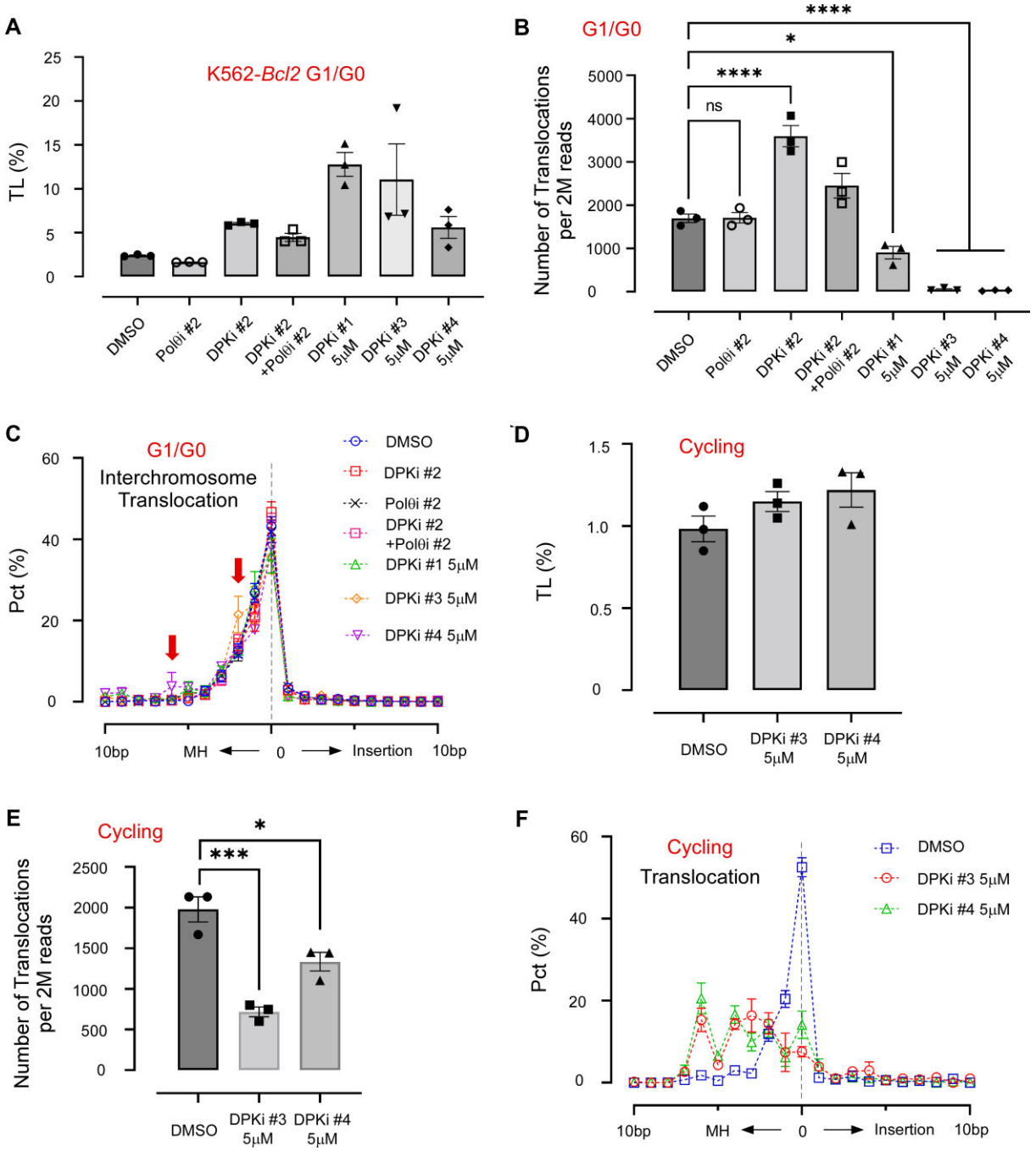

Figure 4. Complete DNA-PKcs inhibition promotes MMEJ-mediated translocations. (**A**) The TL rates between RAG1D and RAG1L sites of G1/G0-arrested *K562-Bcl2* cells upon treatment of DMSO, DNA-PKcs inhibitors DPKi #1–4, Polθi #2 and Polθi #2 + DPKi #2. Note, DPKi #1 was 5 μM, higher than the typical 0.5 μM for default assays. (**B**) The raw number of translocations out of 2 million total reads were shown for each condition and the difference was evaluated by one-way ANOVA plus post-comparison. (**C**) The junction structure in each condition with red arrow indicated the increased microhomology usage. (**D–F**) The two most potent DNA-PKcs inhibitors DPKi #3/4 were further tested in *K562-Bcl2* cycling cells, with (D), (E) and (F) same as (A), (B) and (C), respectively, but for the cycling. All the experiments were independently repeated three times ($n = 3$), and the standard error of the mean (SEM) is indicated, with $^{*}P < 0.05$, $^{***}P < 0.001$, $^{****}P < 0.0001$ and ns (no significance).

(Supplementary Figure S11A) (Supplementary Table S8). The translocation rate was significantly increased in both DNA-PKcs inhibited and deficient cells but were not as severe as *Ku70*$^{-/-}$ cells (Supplementary Figure S11B), supporting the notion of varied NHEJ utilization contributing to signal end baits (63,64). In this regard, junctions from DNA-PKcs inhibited or deficient backgrounds were still predominantly biased for signal end preys and were not substantially resected (Supplementary Figure S11C), nor were the nearly exclusive direct dominant signal end joints affected (Figure 6G and Supplementary Figure S11D, E). It is noteworthy that Vκ junctions from the Jκ5SE bait for all backgrounds assayed appeared to be involved in secondary recombination events from fused RSSs (33,65) since they displayed a

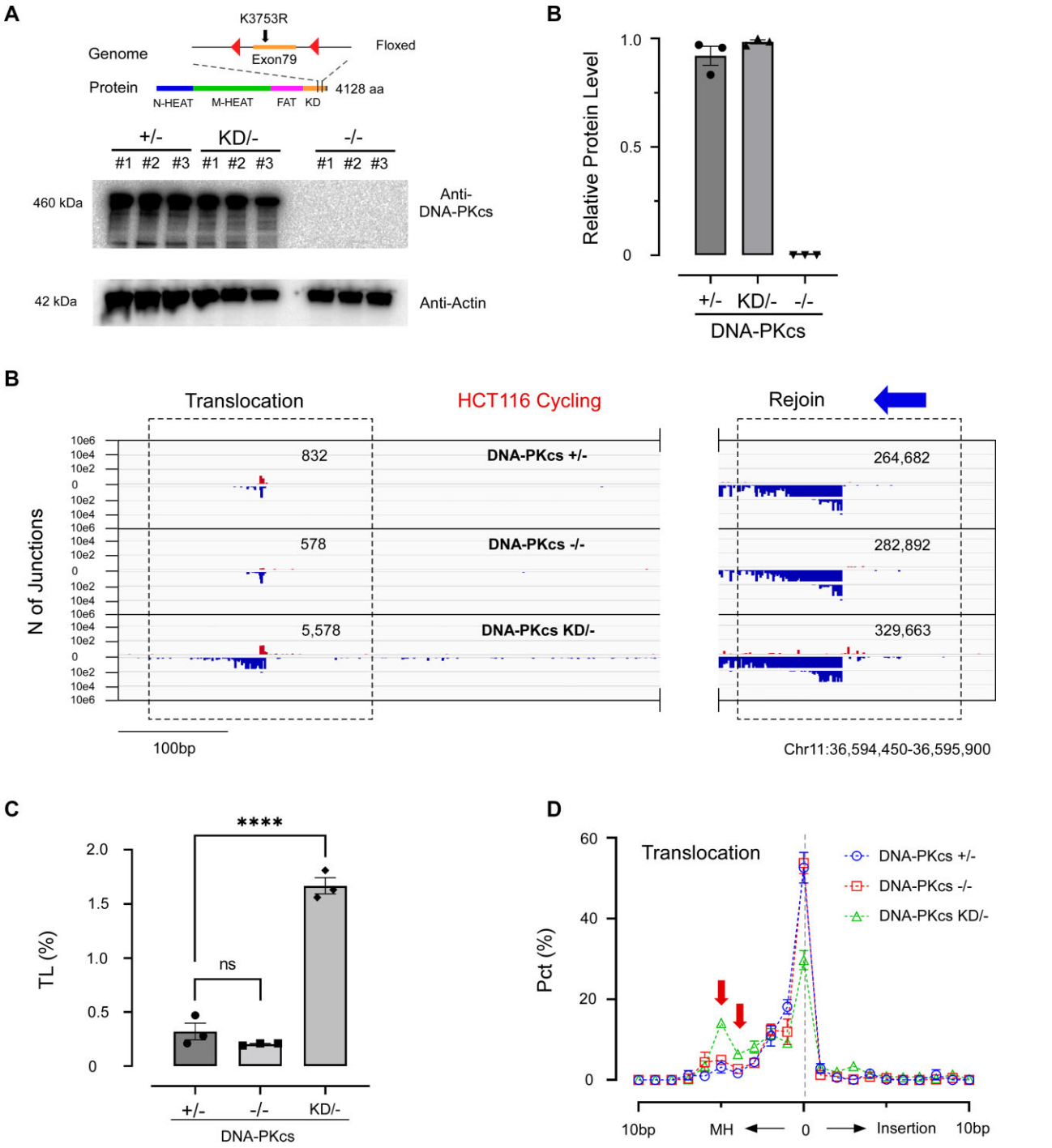

Figure 5. DNA-PKcs kinase dead cells promote MMEJ. (A, B) The exon79 of DNA-PKcs was deleted by flox-cre system and the kinase dead was generated by point mutation on K3753R. The western blot showed comparable level of DNA-PKcs protein in *DNA-PKcs* $^{+/-}$ (control) and *DNA-PKcs* $^{KD/-}$ but absent in *DNA-PKcs* $^{-/-}$ (**A**) and the quantification was provided with error bar (**B**). (**C**) IGV translocation (RAG1D; left) and rejoin (RAG1L; right) plots of HCT116 cycling cells treated with genotypes including *DNA-PKcs* $^{+/-}$ (control), *DNA-PKcs* $^{-/-}$ and *DNA-PKcs* $^{KD/-}$. RAG1L bait priming (blue arrow) is indicated. (**D**) TL rates for *DNA-PKcs* $^{+/-}$, *DNA-PKcs* $^{-/-}$ and *DNA-PKcs* $^{KD/-}$conditions were evaluated one-way ANOVA with $^{****}P < 0.0001$ and ns (no significance). (**E**) Translocation junction structure distributions of the above experiments with red arrows highlighting the increased MH utilization in *DNA-PKcs* $^{KD/-}$ HCT116 cells.

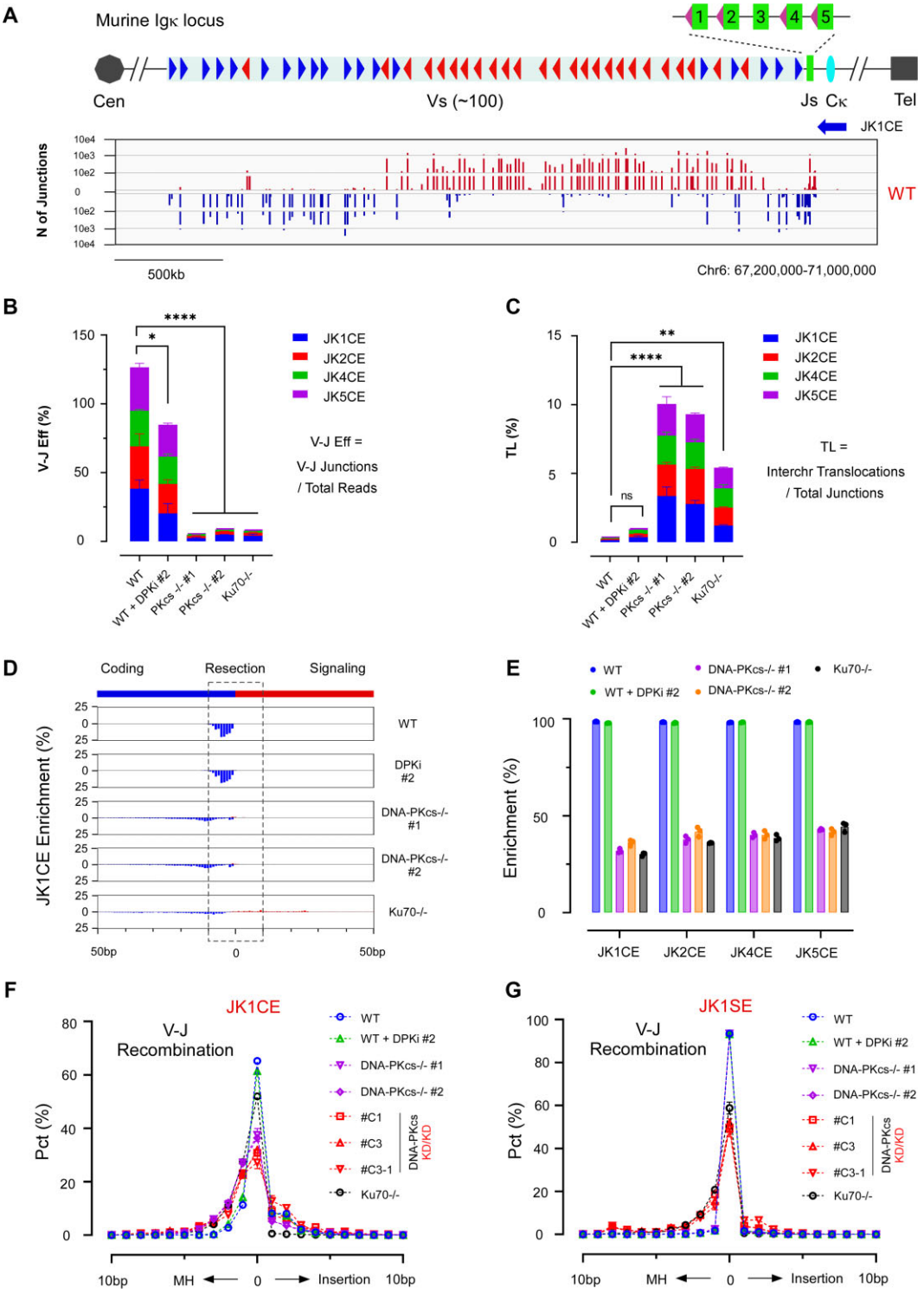

Figure 6. DNA-PKcs protein and kinase status determine V(D)J end joining pathway choice. (**A**) Murine Igκ locus and representative junction profile of *WT v-Abl* cell Vκ-Jκ coding end recombination from the Jκ1 coding end (Jκ1CE) HTGTS bait. Resulting deletions (blue bars) and inversions (red bars) are directed by the RSS orientation. (**B**) V-J Eff (number of Vκ-Jκ junctions divided by the total reads in each library) is indicated for all four functional JκCE baits (Jκ1CE in blue, Jκ2CE in red, Jκ4CE in green, and Jκ5CE in magenta) in stacked bars. Combined values of *WT* (126.57 ± 17.81%), *WT* + DPKi #2 (84.82 ± 12.53%), *DNA-PKcs*$^{-/-}$ #1 (5.00 ± 0.34%), *DNA-PKcs*$^{-/-}$ #2 (8.65 ± 0.25%), and *Ku70*$^{-/-}$ (7.86 ± 1.74%) were evaluated by one-way ANOVA plus Dunnett's posttest. (**C**) Interchromosomal (interchr) translocation fractions (TL Rate; junctions outside chr6 divided by the total junctions) for all four baits are shown in stacked bars. Combined values of *WT* (0.29 ± 0.04%), *WT* + DPKi #2 (0.95 ± 0.13%), *DNA-PKcs*$^{-/-}$ #1 (10.05 ± 1.33%), *DNA*-PKcs$^{-/-}$ #2 (9.31 ± 0.63%), and *Ku70*$^{-/-}$ (5.41 ± 0.37%) were evaluated by one-way ANOVA plus Dunnett's posttest. (**B, C**) $*P < 0.05$; $**P < 0.01$; $****P < 0.0001$; ns, not significant. (**D**) Resected junction plots of the pooled Vκ gene fragment break sites (Jκ1CE bait) within a 100 bp window. RAG breakpoints are at position 0, flanked by coding (blue) and signal (red) sequences, with a 10 bp resection cutoff (dashed box) indicated. (**E**) Junction enrichment within 10 bp of the DSB is quantified and shown for all baits. (**F**) V-J recombined junction structures from the Jκ1CE bait that additionally includes three independently generated DNA-PKcsKD/KD v-Abl clones (#C1, #C3 and #C3-1). (**G**) Same as (**F**) but for the Jκ1SE bait. (B–G) Experiments were independently repeated three times with SEM.

striking loss in signal end bias, substantial increase in resection, and a junction structure pattern resembling coding end joining (Supplementary Figure S11C, F).

Considering the partial inhibition of DPKi #2, we evaluated three DNA-PKcs catalytically dead *v-Abl* cell lines, *DNA-PKcs*$^{KD/KD}$ #C1, #C3 and #C3-1 (D3922A) (39) and examined the genetic inhibition on V(D)J recombination (Supplementary Figure S12A–C) using Jκ1CE and Jκ1SE baits. In general, *DNA-PKcs*$^{KD/KD}$ clones harbored even more functional overlap with *Ku70*$^{-/-}$ than *DNA-PKcs*$^{-/-}$ cells. Specifically, kinase dead clones were ∼1.5% Vκ-Jκ efficient for both bait ends (Supplementary Figure S12A), which was below *Ku70*$^{-/-}$ (∼5–10%) but above *Lig4*$^{-/-}$ (∼0.2–0.4%) (Supplementary Tables S7 and S8) efficiency. Interestingly, and consistent with kinase dead activity in human cells, *DNA-PKcs*$^{KD/KD}$ clones displayed the highest rate of interchromosomal translocation among the *v-Abl* cells assayed (∼5% versus ∼1.5% for *Ku70*$^{-/-}$ Jκ1 baits) (Supplementary Figure S12B). However, V region resected joints displayed an intermediate level of enrichment relative to *WT* and *Ku70*$^{-/-}$, with 70% and 80% junctions within ±10 bp window for Jκ1CE and Jκ1SE baits, respectively (Supplementary Figure S12C); these resected joints were accompanied by a nearly 2-fold drop in direct repair relative to *WT* with increased MMEJ for both baits in a manner mostly resembling *Ku70*$^{-/-}$ (Figure 6F, G). We conclude DNA-PKcs is essential for maintaining the fidelity of Vκ-Jκ recombination by suppressing chromosome translocation.

DNA-PKcs promotes MMEJ in the absence of *Lig4*

Using deeper sequencing and closer nested primer to bait in the *v-Abl* studies described here, we can recover 10x more junctions from *Lig4*$^{-/-}$ RAG DSBs than previously reported, (29) yielding a total junction average of ∼1,800 and ∼1,400 per replication for JκCE and JκSE baits, respectively (Figure 7A; Supplementary Tables S7 and S8). In contrast, *Lig4*$^{-/-}$*Ku70*$^{-/-}$ total junctions averaged ∼10,000 and ∼12,000 per replication for the above baits (Supplementary Tables S7 and S8), yielding >5-fold increase in Vκ-Jκ efficiency (Figure 7B and Supplementary Figure S13A) and were indistinguishable to *Ku70*$^{-/-}$ *v-Abl* cells (30). Thus, we investigated whether DNA-PKcs blocks A-EJ in the *Lig4*$^{-/-}$ context like Ku70. Neither DNA-PKcs inhibition or deletion were found to increase Vκ-Jκ efficiency; in comparison, *Lig4*$^{-/-}$*Ku70*$^{-/-}$ increased Vκ-Jκ efficiency by ∼10-fold (Figure 7B and Supplementary Figure S13A). DNA-PKcs inhibition and deficiency did not increase the already high translocation rate in *Lig4*$^{-/-}$ cells (relative to *WT*), as it does for *Lig4*$^{-/-}$*Ku70*$^{-/-}$ coding end baits (Figure 7C and Supplementary Figure S13B). Overall, the data suggest DNA-PKcs does not block the Ku-independent A-EJ pathway to repair RAG DSBs.

Investigation of resection and junction structures proceeded with Vκ-Jκ junctions. In general, *Lig4*$^{-/-}$ prey resected joints from both JκCE and JκSE baits was greater than *WT* but was less than *Ku70*$^{-/-}$; resected joints were similarly increased in *Lig4*$^{-/-}$*Ku70*$^{-/-}$ cells to a comparable level to *Ku70*$^{-/-}$ alone. DPKi #2 had no added effect on *Lig4*$^{-/-}$ cells (Figure 7D, E and Supplementary Figure S13C), likely due to incomplete inhibition; though we observed only a modest increase in resected joints relative to *WT* with *DNA-PKcs*$^{KD/KD}$ clones (Supplementary Figure S12C) which we infer to be stabilized by the presence of Lig4. Notably for JκCE baits, we observed a decreased range of resected joints with *Lig4*$^{-/-}$*DNA-PKcs*$^{-/-}$ #1/2 clones compared to *Lig4*$^{-/-}$ alone, which aligns with recent studies demonstrating that DNA-PKcs promotes DSB resection (66,67). In JκSE baits, *Lig4*$^{-/-}$*DNA-PKcs*$^{-/-}$ clones displayed varied effects on resection (Supplementary Figure S13C). DNA-PKcs and Ku70 deletion also decreased MMEJ (>2 bp) and correspondingly increased direct repair for all baits compared *Lig4*$^{-/-}$ control (Figure 7F, G, Supplementary Figure S13D–F and S14A–C). Collectively, these findings support a G1/G0-phase NHEJ variant A-EJ pathway that is revealed by Lig4 deficiency and reliant on DNA-PKcs for resection to promote MMEJ.

Discussion

Elucidating the crosstalk between NHEJ and A-EJ mechanisms has been the subject of intense study in recent years. The degree of MMEJ utilization in the resulting joints have been historically used to distinguish NHEJ and A-EJ, (20,21,68–70) however, further investigation was necessary for G1/G0 cells where a recently defined A-EJ mechanism in the absence of Ku70 uses slightly more MMEJ than NHEJ does (29). Our report adds further distinction between DNA-PKcs kinase versus structure functions as it relates to chromosome translocations and MMEJ. Specifically, we found the kinase activity of DNA-PK to be an important step in suppressing translocations, where translocations in human and mouse cells are normally distinguished by direct versus MH joints, respectively repaired by NHEJ and MMEJ (22). On one hand, our data showed complete kinase inhibition led to a block in NHEJ and a rise in MMEJ to varying degrees. The microhomology increase with complete kinase inhibition is aligned with recent findings demonstrating increased MMEJ-mediated translocations (71) or homology-directed repair (57) upon robust DNA-PKcs kinase inhibition.

On the other hand, we delved deeper into the V(D)J recombination consequences of DNA-PKcs perturbations that underlie coding-coding recombination bias via NHEJ and how hybrid (coding-signal) joints are suppressed by DNA-PKcs (Figure 8A), perhaps in collaboration with ATM (72,73). We demonstrated genetic inhibition of DNA-PKcs leads to a more severe shift in the balance between DSB rejoining and translocation than its incomplete chemical inhibition or deficiency, and results in ∼100-fold drop in Vκ-Jκ joining fidelity (Figure 8B, C, Supplementary Tables S7 and S8), therefore, enabling transient kinase inhibition as the driving mechanism to swap synapsed DNA end partners and re-engage NHEJ for efficient repair. In this regard, proximal and frequent DSBs would be highly selected end partners for translocation (30) and, therefore, ideal for enhancing gene edited deletions. Thus, in addition to the 20 to 50-fold increased expression of DNA-PKcs in humans versus mice, (74,75) kinase activity, likely related to autophosphorylation, (39,63) is another contributing factor in the differential manifestation of chromosome translocations between humans and mice. While yet to be tested in mice, a recent report of a novel ATM-mediated phosphorylation site at the extreme C terminal end of DNA-PKcs (T4102) which helps to enhance overall DNA-PKcs functions, specifically stabilizing the DNA-PKcs-Ku interaction and recruitment of processing factors, (76) may bring further insight into NHEJ transition and translocation mechanisms. Despite the end-joining choice, DNA-PKcs suppresses chromosome translocation in both mammals.

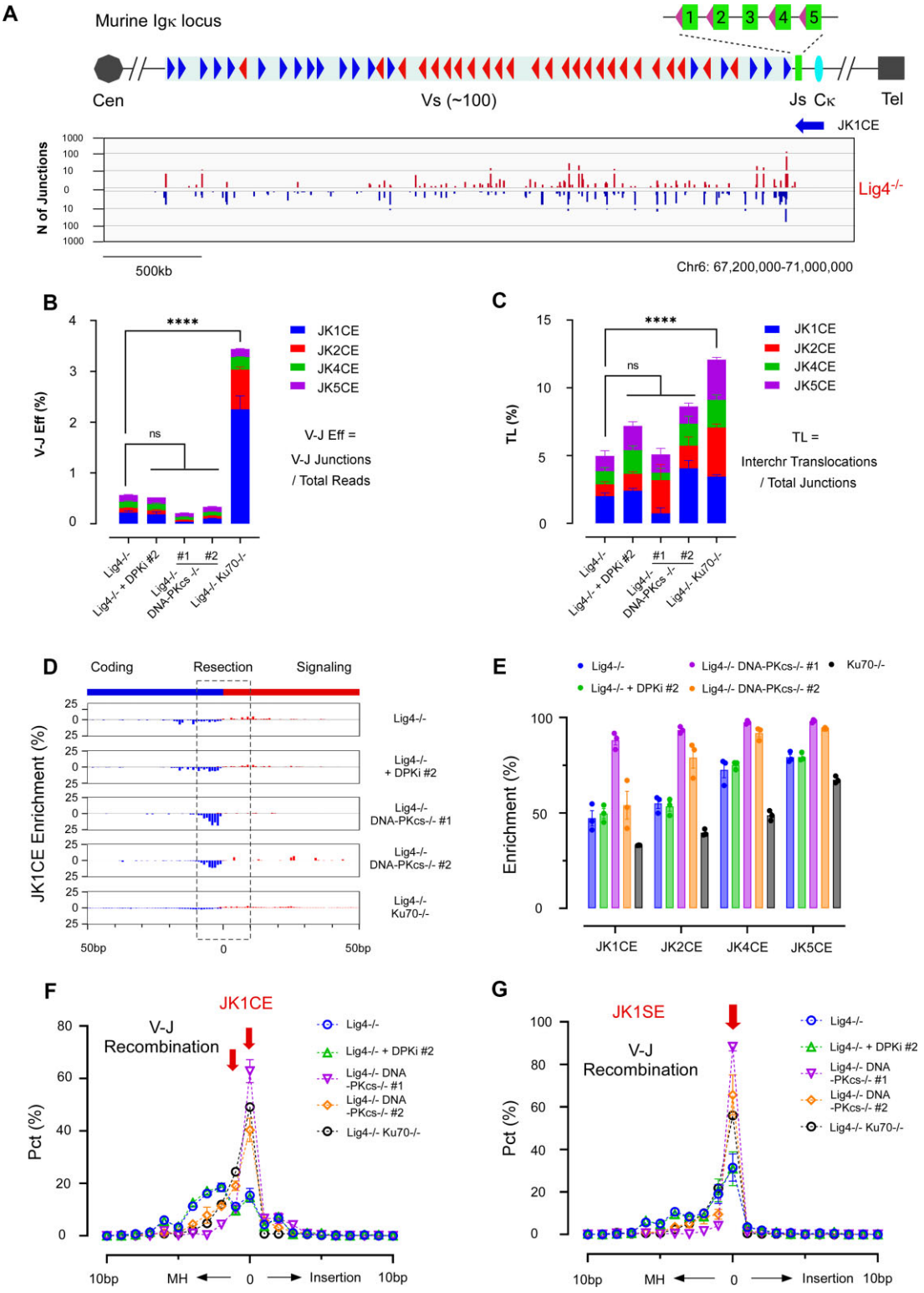

Figure 7. DNA-PKcs promotes MMEJ without Lig4. (**A**) Representative profile of Vκ-Jκ coding ends recombination in *Lig4-/- v-Abl* cells, using the Jκ1CE HTGTS bait. See Figure 5 legend for more details. (**B**) V-J Eff from the four functional Jκ coding end baits are indicated. Combined values of *Lig4-/-* (0.57 ± 0.05%), *Lig4-/-* +DPKi #2 (0.52 ± 0.07%), *Lig4-/- DNA-PKcs*$^{-/-}$ #1 (0.21 ± 0.02%), *Lig4-/- DNA-PKcs*$^{-/-}$ #2 (0.33 ± 0.01%), and *Lig4-/-Ku70*$^{-/-}$ (3.44 ± 0.29%) were statistically distinguished using one-way ANOVA plus Dunnett's posttest. (**C**) Normalized Translocation, TL Rate, are indicated for all four baits. Combined values of Lig4-/- (4.97 ± 0.22%), *Lig4-/-* +DPKi #2 (7.19 ± 0.53%), *Lig4-/- DNA-PKcs*$^{-/-}$ #1 (5.09 ± 1.57%), *Lig4-/- DNA-PKcs-/-* #2 (8.63 ± 1.19%), and *Lig4-/-Ku70*$^{-/-}$ (12.08 ± 0.48%) were distinguished using one-way ANOVA plus Dunnett's posttest. (**B, C**) ****$P < 0.0001$; ns, not significant. (**D**) Resected Vκ region junction plots from Jκ1CE bait are shown; see Figure 5 legend for more details. (**E**) Resected junction summary in all indicated conditions for the four JκCE baits. (**F**) The repair pattern distribution of data with Jκ1CE bait, including microhomology (MH), insertion, and direct repair, in a ±10 bp window in percentage (Pct, %). Red arrows indicate the shift from MH to direct repair in conditions of further *DNA-PKcs*$^{-/-}$ (#1/2) and *Ku70*$^{-/-}$. (**G**) Same as (F) but for Jκ1SE bait. (B–G) Experiments were independently repeated three times with SEM indicated.

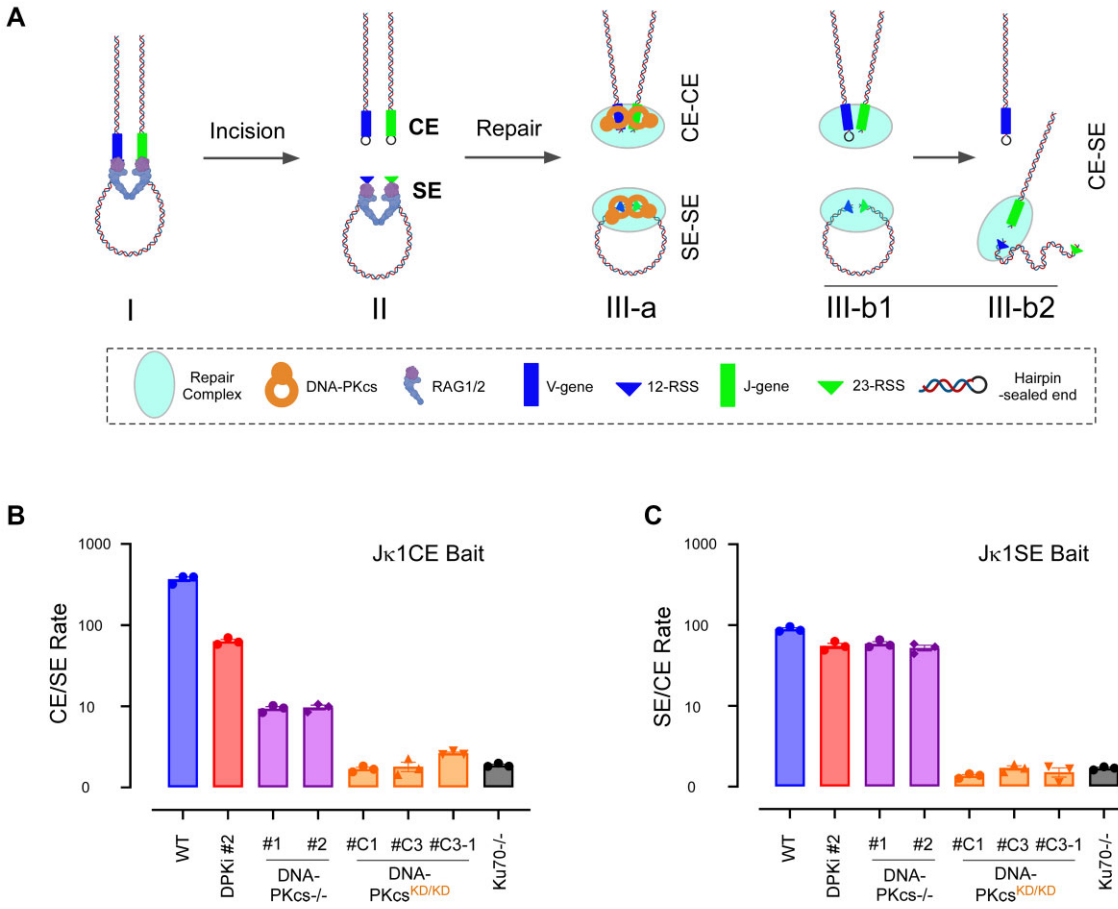

Figure 8. DNA-PKcs suppresses V(D)J recombination infidelity. (**A**) V(D)J recombination fidelity is reliant upon DNA-PKcs protein and kinase activity. Recombination steps: Vκ-Jκ pairing (**I**), RAG1/2-mediated incisions (II), coding-coding (CE–CE) and signal-signal (SE-SE) end synapsis and repair in the presence of DNA-PKcs (III-a). Without DNA-PKcs or kinase activity (not shown), CEs and SEs join each other using A-EJ (III-b1,2). (B, C) Coding end (**B**) and signal end (**C**) bias are progressively lost with DNA-PKcs perturbations: DPKi #2, DNA-PKcs$^{-/-}$ (#1/2) and DNA-PKcs$^{KD/KD}$ (#C1, #C3 and #C3-1). Note the rate is in log scale. Experiments were independently repeated three times with SEM indicated. Panel A was created by BioRender.com.

Although the classic NHEJ transition mechanism involves MRE11 endonuclease/exonuclease activity and eviction of Ku70/80 or with DNA-PKcs, (67) this mechanism is typically viewed through the lens of homologous recombination. Our data support the recent growing evidence of a transition mechanism into using MMEJ that involves DNA-PKcs and Lig4 which could provide insight into end joining pathway choice. We found that DNA-PKcs regulates opposing DNA end resection functions for G1/G0-phase RAG DSBs with the presence of Lig4 suppressing, and the absence of Lig4 promoting, resected end joining. Though suppressing resection aligns with excluding A-EJ, promoting resection was surprising and through a mechanism that is not fully understood (66). It is possible that the immature DNA-PK synapsis at DNA ends (64) provides a favorable platform for recruiting DNA polymerases, nucleases, and other factors to support an Artemis & resection-dependent NHEJ mechanism that was previously described in G1, but not G2, phase (77,78). In this regard, ATM kinase can activate Artemis in the presence of an inhibited DNA-PKcs to promote end procesing (39,73) and could be used to re-engage NHEJ-mediated ligation in the presence of Lig4. Thus, our data suggest the signal to stop end process cycling involves Lig4, likely with other NHEJ short range complex components (8,9,63,64). Whether this persistent DNA-PKcs-dependent resection in the absence of Lig4 is related to the Artemis dependent mechanism, and whether this process more broadly represents an NHEJ-variant mechanism to explain MMEJ-mediated translocations in cycling cells, remain to be determined.

Chromosome translocation is a driver for many cancers including leukemias and lymphomas. Therefore, it is crucial to balance the fitness gains of an efficient V(D)J recombination relative to the deleterious impact of translocations. Previous studies demonstrated that chromosome translocations in cycling murine cells are mediated by A-EJ, (20,21) and A-EJ is often suppressed by NHEJ (22,29,50). In agreement, we found DNA-PKcs kinase dead in both humans and mice generated translocations with elevated MMEJ utilization, perhaps due to removal of non-functional DNA-PK by MRE11 (67,79). We highlight the multifunctions of DNA-PKcs in maintaining genome stability and fidelity of V(D)J recombination by regulating chromosome translocation and end joining pathway commitment.

Limitations of the study

LAM-HTGTS platform methodologies (29–31) only measure imperfect repair outcomes and not repair intermediates. Prior work integrated Southern blotting and/or GFP reporters to estimate Cas9 bait DSB cleavage across sam-

ples (29,30). This study continues using GFP, and in lentiviral experiments mCherry, to document experimental endpoints which are reported in Supplementary Tables S5 and S6. In this context, some data sets were linked to indicate plasmid prep batch effects between experimental replication sets which still displayed the same trend; sequence read, recovered junctions and additional parameters can be readily viewed in Supplementary Tables S4, S7 and S8. DNA-PKcs Kinase Dead *v-Abl* clones (39) were derived from mice without a parallel WT control derivation; thus, comparisons in repair patterns were made to other *v-Abl* lines that were clonally-related (29). Although not reported for *v-Abl* and K562 cell lines, (80) HEK293T and HCT116 are mismatch repair deficient due to defects in MLH1; (81,82) additionally, HCT116 harbors MRE11 hypomorphic mutations that destabilizes RAD50 and NBS1 (83). Given that the data presented here suggests DNA-PKcs kinase activity regulates end joining pathway choice, it will be important to understand its role in cancers that elevate A-EJ, (84–86) for instance, such as those that inhibit TGFβ signaling (87).

Data availability

HTGTS data of human and mouse data were submitted to Gene Expression Omnibus (GEO) and publicly available with the following accession numbers: Human GSE232940; Mouse GSE232944; Revised: GSE249453. Other data for determining the boundary of topology-associated domains are publicly available in GEO: Chip-seq for CTCF in K562 cells (GSM749733, GSM935407 and GSM733719); Chip-seq for Rad21 in K562 cells (GSM935319); Chip-seq for CTCF in HEK293 cells (GSE91917 and GSM749687).

Supplementary data

Supplementary Data are available at NAR Online.

Acknowledgements

We thank the Bassik laboratory for the ACOC gRNA library, Ramesh Nair from Stanford Center for Genomics and Personalized Medicine (SCGPM) for his advice on data analysis, and the Stanford Cancer Institute core facilities. We also thank the Davis (UT Southwestern), (38) Zha (Columbia), (39) and Meek (U Michigan) (61) laboratories for their DNA-PKcs kinase dead and/or null reagent human and mouse cell lines. Some of the figures were generated by BioRender.com or adapted from the Integrative Genomics Viewer (igv.org).

Funding

V Foundation for Cancer Research V Scholar Grant [V2019-003 to R.L.F]; American Cancer Society Research Scholar Grant [RSG-23-1038994-01-DMC to R.L.F.]. Funding for open access charge: American Cancer Society.

Conflict of interest statement

None declared.

References

1. Lees-Miller,J.P., Cobban,A., Katsonis,P., Bacolla,A., Tsutakawa,S.E., Hammel,M., Meek,K., Anderson,D.W., Lichtarge,O., Tainer,J.A., *et al.* (2021) Uncovering DNA-PKcs ancient phylogeny, unique sequence motifs and insights for human disease. *Prog. Biophys. Mol. Biol.*, **163**, 87–108.
2. Gottlieb,T.M. and Jackson,S.P. (1993) The DNA-dependent protein kinase: requirement for DNA ends and association with Ku antigen. *Cell*, **72**, 131–142.
3. Lees-Miller,S.P., Godbout,R., Chan,D.W., Weinfeld,M., Day,R.S., Barron,G.M. and Allalunis-Turner,J. (1995) Absence of p350 subunit of DNA-activated protein kinase from a radiosensitive human cell line. *Science*, **267**, 1183–1185.
4. Peterson,S.R., Kurimasa,A., Oshimura,M., Dynan,W.S., Bradbury,E.M. and Chen,D.J. (1995) Loss of the catalytic subunit of the DNA-dependent protein kinase in DNA double-strand-break-repair mutant mammalian cells. *Proc. Natl. Acad. Sci. U.S.A.*, **92**, 3171–3174.
5. Graham,T.G., Walter,J.C. and Loparo,J.J. (2016) Two-stage synapsis of DNA ends during non-homologous end joining. *Mol. Cell*, **61**, 850–858.
6. Wang,J.L., Duboc,C., Wu,Q., Ochi,T., Liang,S., Tsutakawa,S.E., Lees-Miller,S.P., Nadal,M., Tainer,J.A., Blundell,T.L., *et al.* (2018) Dissection of DNA double-strand-break repair using novel single-molecule forceps. *Nat. Struct. Mol. Biol.*, **25**, 482–487.
7. Chaplin,A.K., Hardwick,S.W., Liang,S., Kefala Stavridi,A., Hnizda,A., Cooper,L.R., De Oliveira,T.M., Chirgadze,D.Y. and Blundell,T.L. (2021) Dimers of DNA-PK create a stage for DNA double-strand break repair. *Nat. Struct. Mol. Biol.*, **28**, 13–19.
8. Chen,S., Lee,L., Naila,T., Fishbain,S., Wang,A., Tomkinson,A.E., Lees-Miller,S.P. and He,Y. (2021) Structural basis of long-range to short-range synaptic transition in NHEJ. *Nature*, **593**, 294–298.
9. Chaplin,A.K., Hardwick,S.W., Stavridi,A.K., Buehl,C.J., Goff,N.J., Ropars,V., Liang,S., De Oliveira,T.M., Chirgadze,D.Y., Meek,K., *et al.* (2021) Cryo-EM of NHEJ supercomplexes provides insights into DNA repair. *Mol. Cell*, **81**, 3400–3409.
10. Zhao,B., Watanabe,G., Morten,M.J., Reid,D.A., Rothenberg,E. and Lieber,M.R. (2019) The essential elements for the noncovalent association of two DNA ends during NHEJ synapsis. *Nat. Commun.*, **10**, 3588.
11. Park,E.J., Chan,D.W., Park,J.H., Oettinger,M.A. and Kwon,J. (2003) DNA-PK is activated by nucleosomes and phosphorylates H2AX within the nucleosomes in an acetylation-dependent manner. *Nucleic. Acids. Res.*, **31**, 6819–6827.
12. Mukherjee,B., Kessinger,C., Kobayashi,J., Chen,B.P., Chen,D.J., Chatterjee,A. and Burma,S. (2006) DNA-PK phosphorylates histone H2AX during apoptotic DNA fragmentation in mammalian cells. *DNA Repair (Amst.)*, **5**, 575–590.
13. An,J., Huang,Y.C., Xu,Q.Z., Zhou,L.J., Shang,Z.F., Huang,B., Wang,Y., Liu,X.D., Wu,D.C. and Zhou,P.K. (2010) DNA-PKcs plays a dominant role in the regulation of H2AX phosphorylation in response to DNA damage and cell cycle progression. *BMC Mol. Biol.*, **11**, 18.
14. Chiarle,R., Zhang,Y., Frock,R.L., Lewis,S.M., Molinie,B., Ho,Y.J., Myers,D.R., Choi,V.W., Compagno,M., Malkin,D.J., *et al.* (2011) Genome-wide translocation sequencing reveals mechanisms of chromosome breaks and rearrangements in B cells. *Cell*, **147**, 107–119.
15. Roukos,V. and Misteli,T. (2014) The biogenesis of chromosome translocations. *Nat. Cell Biol.*, **16**, 293–300.
16. Ramsden,D.A. and Nussenzweig,A. (2021) Mechanisms driving chromosomal translocations: lost in time and space. *Oncogene*, **40**, 4263–4270.
17. Roukos,V., Voss,T.C., Schmidt,C.K., Lee,S., Wangsa,D. and Misteli,T. (2013) Spatial dynamics of chromosome translocations in living cells. *Science*, **341**, 660–664.
18. Franco,S., Murphy,M.M., Li,G., Borjeson,T., Boboila,C. and Alt,F.W. (2008) DNA-PKcs and artemis function in the end-joining

phase of immunoglobulin heavy chain class switch recombination. *J. Exp. Med.*, **205**, 557–564.
19. Callén,E., Jankovic,M., Wong,N., Zha,S., Chen,H.T., Difilippantonio,S., Di Virgilio,M., Heidkamp,G., Alt,F.W., Nussenzweig,A., *et al.* (2009) Essential role for DNA-PKcs in DNA double-strand break repair and apoptosis in ATM-deficient lymphocytes. *Mol. Cell*, **34**, 285–297.
20. Simsek,D., Brunet,E., Wong,S.Y., Katyal,S., Gao,Y., McKinnon,P.J., Lou,J., Zhang,L., Li,J., Rebar,E.J., *et al.* (2011) DNA ligase III promotes alternative nonhomologous end-joining during chromosomal translocation formation. *PLoS Genet.*, **7**, e1002080.
21. Zhang,Y. and Jasin,M. (2011) An essential role for CtIP in chromosomal translocation formation through an alternative end-joining pathway. *Nat. Struct. Mol. Biol.*, **18**, 80–84.
22. Ghezraoui,H., Piganeau,M., Renouf,B., Renaud,J.B., Sallmyr,A., Ruis,B., Oh,S., Tomkinson,A.E., Hendrickson,E.A., Giovannangeli,C., *et al.* (2014) Chromosomal translocations in human cells are generated by canonical nonhomologous end-joining. *Mol. Cell*, **55**, 829–842.
23. Zhang,Y., Zhang,X., Dai,H.Q., Hu,H. and Alt,F.W. (2022) The role of chromatin loop extrusion in antibody diversification. *Nat. Rev. Immunol.*, **22**, 550–566.
24. Ma,Y., Pannicke,U., Schwarz,K. and Lieber,M.R. (2002) Hairpin opening and overhang processing by an Artemis/DNA-dependent protein kinase complex in nonhomologous end joining and V(D)J recombination. *Cell*, **108**, 781–794.
25. Gao,Y., Chaudhuri,J., Zhu,C., Davidson,L., Weaver,D.T. and Alt,F.W. (1998) A targeted DNA-PKcs-null mutation reveals DNA-PK-independent functions for KU in V(D)J recombination. *Immunity*, **9**, 367–376.
26. Taccioli,G.E., Amatucci,A.G., Beamish,H.J., Gell,D., Xiang,X.H., Torres Arzayus,M.I., Priestley,A., Jackson,S.P., Marshak Rothstein,A., Jeggo,P.A., *et al.* (1998) Targeted disruption of the catalytic subunit of the DNA-PK gene in mice confers severe combined immunodeficiency and radiosensitivity. *Immunity*, **9**, 355–366.
27. Kurimasa,A., Ouyang,H., Dong,L.J., Wang,S., Li,X., Cordon-Cardo,C., Chen,D.J. and Li,G.C. (1999) Catalytic subunit of DNA-dependent protein kinase: impact on lymphocyte development and tumorigenesis. *Proc. Natl. Acad. Sci. U.S.A.*, **96**, 1403–1408.
28. Zha,S., Jiang,W., Fujiwara,Y., Patel,H., Goff,P.H., Brush,J.W., Dubois,R.L. and Alt,F.W. (2011) Ataxia telangiectasia-mutated protein and DNA-dependent protein kinase have complementary V(D)J recombination functions. *Proc. Natl. Acad. Sci. U.S.A.*, **108**, 2028–2033.
29. Liang,Z., Kumar,V., Le Bouteiller,M., Zurita,J., Kenrick,J., Lin,S.G., Lou,J., Hu,J., Ye,A.Y., Boboila,C., *et al.* (2021) Ku70 suppresses alternative end joining in G1-arrested progenitor B cells. *Proc. Natl. Acad. Sci. U.S.A.*, **118**, e2103630118.
30. Frock,R.L., Hu,J., Meyers,R.M., Ho,Y.J., Kii,E. and Alt,F.W. (2015) Genome-wide detection of DNA double-stranded breaks induced by engineered nucleases. *Nat. Biotechnol.*, **33**, 179–186.
31. Hu,J., Meyers,R.M., Dong,J., Panchakshari,R.A., Alt,F.W. and Frock,R.L. (2016) Detecting DNA double-stranded breaks in mammalian genomes by linear amplification-mediated high-throughput genome-wide translocation sequencing. *Nat. Protoc.*, **11**, 853–871.
32. Lin,S.G., Ba,Z., Du,Z., Zhang,Y., Hu,J. and Alt,F.W. (2016) Highly sensitive and unbiased approach for elucidating antibody repertoires. *Proc. Natl. Acad. Sci. U.S.A.*, **113**, 7846–7851.
33. Zhao,L., Frock,R.L., Du,Z., Hu,J., Chen,L., Krangel,M.S. and Alt,F.W. (2016) Orientation-specific RAG activity in chromosomal loop domains contributes to tcrd V(D)J recombination during T cell development. *J. Exp. Med.*, **213**, 1921–1936.
34. Dai,H.Q., Hu,H., Lou,J., Ye,A.Y., Ba,Z., Zhang,X., Zhang,Y., Zhao,L., Yoon,H.S., Chapdelaine-Williams,A.M., *et al.* (2021) Loop extrusion mediates physiological igh locus contraction for RAG scanning. *Nature*, **590**, 338–343.
35. Cao,J., Wu,L., Zhang,S.M., Lu,M., Cheung,W.K., Cai,W., Gale,M., Xu,Q. and Yan,Q. (2016) An easy and efficient inducible CRISPR/Cas9 platform with improved specificity for multiple gene targeting. *Nucleic Acids Res.*, **44**, e149.
36. Han,K., Jeng,E.E., Hess,G.T., Morgens,D.W., Li,A. and Bassik,M.C. (2017) Synergistic drug combinations for cancer identified in a CRISPR screen for pairwise genetic interactions. *Nat. Biotechnol.*, **35**, 463–474.
37. Morgens,D.W., Wainberg,M., Boyle,E.A., Ursu,O., Araya,C.L., Tsui,C.K., Haney,M.S., Hess,G.T., Han,K., Jeng,E.E., *et al.* (2017) Genome-scale measurement of off-target activity using Cas9 toxicity in high-throughput screens. *Nat. Commun.*, **8**, 15178.
38. Lu,H., Saha,J., Beckmann,P.J., Hendrickson,E.A. and Davis,A.J. (2019) DNA-PKcs promotes chromatin decondensation to facilitate initiation of the DNA damage response. *Nucleic Acids Res.*, **47**, 9467–9479.
39. Jiang,W., Crowe,J.L., Liu,X., Nakajima,S., Wang,Y., Li,C., Lee,B.J., Dubois,R.L., Liu,C., Yu,X., *et al.* (2015) Differential phosphorylation of DNA-PKcs regulates the interplay between end-processing and end-ligation during nonhomologous end-joining. *Mol. Cell*, **58**, 172–185.
40. Leahy,J.J., Golding,B.T., Griffin,R.J., Hardcastle,I.R., Richardson,C., Rigoreau,L. and Smith,G.C. (2004) Identification of a highly potent and selective DNA-dependent protein kinase (DNA-PK) inhibitor (NU7441) by screening of chromenone libraries. *Bioorg. Med. Chem. Lett.*, **14**, 6083–6087.
41. Willmore,E., de Caux,S., Sunter,N.J., Tilby,M.J., Jackson,G.H., Austin,C.A. and Durkacz,B.W. (2004) A novel DNA-dependent protein kinase inhibitor, NU7026, potentiates the cytotoxicity of topoisomerase II poisons used in the treatment of leukemia. *Blood*, **103**, 4659–4665.
42. Damstrup,L., Zimmerman,A., Sirrenberg,C., Zenke,F. and Vassilev,L. (2016) M3814, a DNA-dependent protein kinase inhibitor (DNA-PKi), potentiates the effect of ionizing radiation (IR) in xenotransplanted tumors in nude mice. *Int. J. Radiat. Oncol. Biol. Phys.*, **94**, 940–941.
43. Khan,A.J., Misenko,S.M., Thandoni,A., Schiff,D., Jhawar,S.R., Bunting,S.F. and Haffty,B.G. (2018) VX-984 is a selective inhibitor of non-homologous end joining, with possible preferential activity in transformed cells. *Oncotarget*, **9**, 25833–25841.
44. Fok,J.H.L., Ramos-Montoya,A., Vazquez-Chantada,M., Wijnhoven,P.W.G., Follia,V., James,N., Farrington,P.M., Karmokar,A., Willis,S.E., Cairns,J., *et al.* (2019) AZD7648 is a potent and selective DNA-PK inhibitor that enhances radiation, chemotherapy and olaparib activity. *Nat. Commun.*, **10**, 5065.
45. Taylor,A.M., Metcalfe,J.A., Thick,J. and Mak,Y.F. (1996) Leukemia and lymphoma in ataxia telangiectasia. *Blood*, **87**, 423–438.
46. Golding,S.E., Rosenberg,E., Valerie,N., Hussaini,I., Frigerio,M., Cockcroft,X.F., Chong,W.Y., Hummersone,M., Rigoreau,L., Menear,K.A., *et al.* (2009) Improved ATM kinase inhibitor KU-60019 radiosensitizes glioma cells, compromises insulin, AKT and ERK prosurvival signaling, and inhibits migration and invasion. *Mol. Cancer Ther.*, **8**, 2894–2902.
47. Finn,R.S., Martin,M., Rugo,H.S., Jones,S., Im,S.A., Gelmon,K., Harbeck,N., Lipatov,O.N., Walshe,J.M., Moulder,S., *et al.* (2016) Palbociclib and Letrozole in advanced breast cancer. *N. Engl. J. Med.*, **375**, 1925–1936.
48. Guiley,K.Z., Stevenson,J.W., Lou,K., Barkovich,K.J., Kumarasamy,V., Wijeratne,T.U., Bunch,K.L., Tripathi,S., Knudsen,E.S., Witkiewicz,A.K., *et al.* (2019) p27 allosterically activates cyclin-dependent kinase 4 and antagonizes palbociclib inhibition. *Science*, **366**, eaaw2106.
49. Wang,J., Le Gall,J., Frock,R.L. and Strick,T.R. (2023) Shifted PAMs generate DNA overhangs and enhance SpCas9 post-catalytic complex dissociation. *Nat. Struct. Mol. Biol.*, **30**, 1707–1718.
50. Wang,M., Wu,W., Wu,W., Rosidi,B., Zhang,L., Wang,H. and Iliakis,G. (2006) PARP-1 and Ku compete for repair of DNA

double strand breaks by distinct NHEJ pathways. *Nucleic Acids Res*., **34**, 6170–6182.
51. Mansour,W.Y., Rhein,T. and Dahm-Daphi,J. (2010) The alternative end-joining pathway for repair of DNA double-strand breaks requires PARP1 but is not dependent upon microhomologies. *Nucleic Acids Res*., **38**, 6065–6077.
52. Chan,S.H., Yu,A.M. and McVey,M. (2010) Dual roles for DNA polymerase theta in alternative end-joining repair of double-strand breaks in Drosophila. *PLoS Genet*., **6**, e1001005.
53. Menear,K.A., Adcock,C., Boulter,R., Cockcroft,X.L., Copsey,L., Cranston,A., Dillon,K.J., Drzewiecki,J., Garman,S., Gomez,S., *et al.* (2008) 4-[3-(4-cyclopropanecarbonylpiperazine-1-carbonyl)-4-fluorobenzyl]-2H-phthalazin-1-one: a novel bioavailable inhibitor of poly(ADP-ribose) polymerase-1. *J. Med. Chem*.,, **51**, 6581–6591.
54. Zhou,J., Gelot,C., Pantelidou,C., Li,A., Yücel,H., Davis,R.E., Färkkilä,A., Kochupurakkal,B., Syed,A., Shapiro,G.I., *et al.* (2021) A first-in-class Polymerase Theta inhibitor selectively targets homologous-recombination-deficient tumors. *Nat. Cancer*, **2**, 598–610.
55. Arnould,C., Rocher,V., Finoux,A.L., Clouaire,T., Li,K., Zhou,F., Caron,P., Mangeot,P.E., Ricci,E.P., Mourad,R., *et al.* (2021) Loop extrusion as a mechanism for formation of DNA damage repair foci. *Nature*, **590**, 660–665.
56. Liang,S., Thomas,S.E., Chaplin,A.K., Hardwick,S.W., Chirgadze,D.Y. and Blundell,T.L. (2022) Structural insights into inhibitor regulation of the DNA repair protein DNA-PKcs. *Nature*, **601**, 643–648.
57. Selvaraj,S., Feist,W.N., Viel,S., Vaidyanathan,S., Dudek,A.M., Gastou,M., Rockwood,S.J., Ekman,F.K., Oseghale,A.R., Xu,L., *et al.* (2023) High-efficiency transgene integration by homology-directed repair in human primary cells using DNA-PKcs inhibition. *Nat. Biotechnol*., https://doi.org/10.1038/s41587-023-01888-4.
58. Anne Esguerra,Z., Watanabe,G., Okitsu,C.Y., Hsieh,C.L. and Lieber,M.R. (2020) DNA-PKcs chemical inhibition versus genetic mutation: impact on the junctional repair steps of V(D)J recombination. *Mol. Immunol*., **120**, 93–100.
59. Pismataro,M.C., Astolfi,A., Barreca,M.L., Pacetti,M., Schenone,S., Bandiera,T., Carbone,A. and Massari,S. (2023) Small molecules targeting DNA polymerase theta (POLθ) as promising synthetic lethal agents for precision cancer therapy. *J. Med. Chem*., **66**, 6498–6522.
60. Ruis,B.L., Fattah,K.R. and Hendrickson,E.A. (2008) The catalytic subunit of DNA-dependent protein kinase regulates proliferation, telomere length, and genomic stability in human somatic cells. *Mol. Cell. Biol*., **28**, 6182–6195.
61. Neal,J.A. and Meek,K. (2019) Deciphering phenotypic variance in different models of DNA-PKcs deficiency. *DNA Repair (Amst.)*, **73**, 7–16.
62. Oksenych,V., Kumar,V., Liu,X., Guo,C., Schwer,B., Zha,S. and Alt,F.W. (2013) Functional redundancy between the XLF and DNA-PKcs DNA repair factors in V(D)J recombination and nonhomologous DNA end joining. *Proc. Natl. Acad. Sci. U.S.A*., **110**, 2234–2239.
63. Liu,L., Chen,X., Li,J., Wang,H., Buehl,C.J., Goff,N.J., Meek,K., Yang,W. and Gellert,M. (2022) Autophosphorylation transforms DNA-PK from protecting to processing DNA ends. *Mol. Cell*, **82**, 177–189.
64. Buehl,C.J., Goff,N.J., Hardwick,S.W., Gellert,M., Blundell,T.L., Yang,W., Chaplin,A.K. and Meek,K. (2023) Two distinct long-range synaptic complexes promote different aspects of end processing prior to repair of DNA breaks by non-homologous end joining. *Mol. Cell*, **83**, 698–714.
65. Hu,J., Zhang,Y., Zhao,L., Frock,R.L., Du,Z., Meyers,R.M., Meng,F.L., Schatz,D.G. and Alt,F.W. (2015) Chromosomal loop domains direct the recombination of antigen receptor genes. *Cell*, **163**, 947–959.
66. Fowler,F.C., Chen,B.R., Zolnerowich,N., Wu,W., Pavani,R., Paiano,J., Peart,C., Chen,Z., Nussenzweig,A., Sleckman,B.P., *et al.* (2022) DNA-PK promotes DNA end resection at DNA double strand breaks in G_0 cells. *eLife*, **11**, e74700.
67. Deshpande,R.A., Myler,L.R., Soniat,M.M., Makharashvili,N., Lee,L., Lees-Miller,S.P., Finkelstein,I.J. and Paull,T.T. (2020) DNA-dependent protein kinase promotes DNA end processing by MRN and CtIP. *Sci. Adv*., **6**, eaay0922.
68. Chang,H.H.Y., Pannunzio,N.R., Adachi,N. and Lieber,M.R. (2017) Non-homologous DNA end joining and alternative pathways to double-strand break repair. *Nat. Rev. Mol. Cell Biol*.,**18**, 495–506.
69. Sallmyr,A. and Tomkinson,A.E. (2018 Jul 6) Repair of DNA double-strand breaks by mammalian alternative end-joining pathways. *J. Biol. Chem*., **293**, 10536–10546.
70. Zhao,B., Rothenberg,E., Ramsden,D.A. and Lieber,M.R. (2020) The molecular basis and disease relevance of non-homologous DNA end joining. *Nat. Rev. Mol. Cell Biol*., **21**, 765–781.
71. Zagelbaum,J., Schooley,A., Zhao,J., Schrank,B.R., Callen,E., Zha,S., Gottesman,M.E., Nussenzweig,A., Rabadan,R., Dekker,J., *et al.* (2023) Multiscale reorganization of the genome following DNA damage facilitates chromosome translocations via nuclear actin polymerization. *Nat. Struct. Mol. Biol*., **30**, 99–106.
72. Riballo,E., Kühne,M., Rief,N., Doherty,A., Smith,G.C., Recio,M.J., Reis,C., Dahm,K., Fricke,A., Krempler,A., *et al.* (2004) A pathway of double-strand break rejoining dependent upon ATM, Artemis, and proteins locating to gamma-H2AX foci. *Mol. Cell*, **16**, 715–724.
73. Bredemeyer,A.L., Huang,C.Y., Walker,L.M., Bassing,C.H. and Sleckman,B.P. (2008) Aberrant V(D)J recombination in ataxia telangiectasia mutated-deficient lymphocytes is dependent on nonhomologous DNA end joining. *J. Immunol*., **181**, 2620–2625.
74. Finnie,N.J., Gottlieb,T.M., Blunt,T., Jeggo,P.A. and Jackson,S.P. (1995) DNA-dependent protein kinase activity is absent in xrs-6 cells: implications for site-specific recombination and DNA double-strand break repair. *Proc. Natl. Acad. Sci. U.S.A*.,, **92**, 320–324.
75. Jiang,W., Estes,V.M., Wang,X.S., Shao,Z., Lee,B.J., Lin,X., Crowe,J.L. and Zha,S. (2019) Phosphorylation at S2053 in murine (S2056 in Human) DNA-PKcs is dispensable for lymphocyte development and class switch recombination. *J. Immunol*., **203**, 178–187.
76. Lu,H., Zhang,Q., Laverty,D.J., Puncheon,A.C., Augustine,M.M., Williams,G.J., Nagel,Z.D., Chen,B.P.C. and Davis,A.J. (2023) ATM phosphorylates the FATC domain of DNA-PKcs at threonine 4102 to promote non-homologous end joining. *Nucleic Acids Res*., **51**, 6770–6783.
77. Biehs,R., Steinlage,M., Barton,O., Juhász,S., Künzel,J., Spies,J., Shibata,A., Jeggo,P.A. and Löbrich,M. (2017) DNA double-strand break resection occurs during non-homologous end joining in G1 but is distinct from resection during homologous recombination. *Mol. Cell*, **65**, 671–684.
78. Frock,R.L., Sadeghi,C., Meng,J. and Wang,J.L. (2021) DNA end joining: g0-ing to the core. *Biomolecules*, **11**, 1487.
79. Deshpande,R.A., Marin-Gonzalez,A., Barnes,H.K., Woolley,P.R., Ha,T. and Paull,T.T. (2023) Genome-wide analysis of DNA-PK-bound MRN cleavage products supports a sequential model of DSB repair pathway choice. *Nat. Commun*., **14**, 5759.
80. Matheson,E.C. and Hall,A.G. (2003) Assessment of mismatch repair function in leukaemic cell lines and blasts from children with acute lymphoblastic leukaemia. *Carcinogenesis*, **24**, 31–38.
81. Panigrahi,G.B., Slean,M.M., Simard,J.P. and Pearson,C.E. (2012) Human mismatch repair protein hMutLα is required to repair short slipped-DNAs of trinucleotide repeats. *J. Biol. Chem*., **287**, 41844–41850.
82. Imesch,P., Goerens,A., Fink,D. and Fedier,A. (2012) MLH1-deficient HCT116 colon tumor cells exhibit resistance to the cytostatic and cytotoxic effect of the poly(A) polymerase

inhibitor cordycepin (3'-deoxyadenosine) in vitro. *Oncol. Lett.*, **3**, 441–444.
83. Takemura,H., Rao,V.A., Sordet,O., Furuta,T., Miao,Z.H., Meng,L., Zhang,H. and Pommier,Y. (2006) Defective Mre11-dependent activation of Chk2 by ataxia telangiectasia mutated in colorectal carcinoma cells in response to replication-dependent DNA double strand breaks. *J. Biol. Chem.*, **281**, 30814–30823.
84. Ceccaldi,R., Liu,J.C., Amunugama,R., Hajdu,I., Primack,B., Petalcorin,M.I., O'Connor,K.W., Konstantinopoulos,P.A., Elledge,S.J., Boulton,S.J., *et al.* (2015) Homologous-recombination-deficient tumours are dependent on Polθ-mediated repair. *Nature*, **518**, 258–262.
85. Tobin,L.A., Robert,C., Nagaria,P., Chumsri,S., Twaddell,W., Ioffe,O.B., Greco,G.E., Brodie,A.H. and Tomkinson,A.E., (2012) Rassool FV. Targeting abnormal DNA repair in therapy-resistant breast cancers. *Mol. Cancer Res.*, **10**, 96–107.
86. Newman,E.A., Lu,F., Bashllari,D., Wang,L., Opipari,A.W. and Castle,V.P. (2015) Alternative NHEJ pathway components are therapeutic targets in high-risk neuroblastoma. *Mol. Cancer Res.*, **13**, 470–482.
87. Liu,Q., Palomero,L., Moore,J., Guix,I., Espín,R., Aytés,A., Mao,J.H., Paulovich,A.G., Whiteaker,J.R., Ivey,R.G., *et al.* (2021) Loss of tgfβ signaling increases alternative end-joining DNA repair that sensitizes to genotoxic therapies across cancer types. *Sci. Transl. Med.*, **13**, eabc4465.

Received: July 11, 2023. **Revised:** February 9, 2024. **Editorial Decision:** February 12, 2024. **Accepted:** February 14, 2024